

Quadrant polarization parameters for the scattered light of circumstellar disks.

Analysis of debris disk models and observations of HR 4796A

H.M. Schmid

ETH Zurich, Institute for Particle Physics and Astrophysics, Wolfgang-Pauli-Strasse 27, CH-8093 Zurich, Switzerland,
e-mail: schmid@astro.phys.ethz.ch

Received ...; accepted ...

ABSTRACT

Context. Modern imaging polarimetry provides spatially resolved observations for many circumstellar disks and quantitative results for the measured polarization which can be used for comparisons with model calculations and for systematic studies of disk samples.

Aims. This paper introduces the quadrant polarization parameters Q_{000} , Q_{090} , Q_{180} , Q_{270} for Stokes Q and U_{045} , U_{135} , U_{225} , U_{315} for Stokes U for circumstellar disks and describes their use for the polarimetric characterization of the dust in debris disks.

Methods. We define the quadrant polarization parameters Q_{xxx} and U_{xxx} and illustrate their properties with measurements of the debris disk around HR 4796A from Milli et al. (2019). We calculate quadrant parameters for simple models of rotationally symmetric and optically thin debris disks and the results provide diagnostic diagrams for the determination of the scattering asymmetry of the dust. This method is tested with data for HR 4796A and compared with detailed scattering phase curve extractions in the literature.

Results. The parameters Q_{xxx} and U_{xxx} are ideal for a well-defined and simple characterization of the azimuthal dependence of the polarized light from circumstellar disk because they are based on the “natural” Stokes Q and U quadrant pattern produced by circumstellar scattering. For optically thin and rotationally symmetric debris disks the quadrant parameters normalized to the integrated azimuthal polarization Q_{xxx}/Q_ϕ and U_{xxx}/Q_ϕ or quadrant ratios like Q_{000}/Q_{180} depend only on the disk inclination i and the polarized scattering phase function $f_\phi(\theta)$ of the dust, and they do not depend on the radial distribution of the scattering emissivity. Because the disk inclination i is usually well known for resolved observations, we can derive the shape of $f_\phi(\theta)$ for the phase angle range θ sampled by the polarization quadrants. This finding also applies to models with vertical extensions as observed for debris disks. Diagnostic diagrams are calculated for all normalized quadrant parameters and several quadrant ratios for the determination of the asymmetry parameter g of the polarized Henyey-Greenstein scattering phase function $f_\phi(\theta, g)$. We apply these diagrams to the measurement of HR 4796A, and find that a phase function with only one parameter does not reproduce the data well. We find a better solution with a three-parameter phase function $f_\phi(\theta, g_1, g_2, w)$, but it is also noted that the well-observed complex disk of HR 4796A cannot be described in full detail with the simple quadrant polarization parameters.

Conclusions. The described quadrant polarization parameters are very useful for quantifying the azimuthal dependence of the scattering polarization of spatially resolved circumstellar disks illuminated by the central star. They provide a simple test of the deviations of the disk geometry from axisymmetry and can be used to constrain the scattering phase function for optically thin disks without detailed model fitting of disk images. The parameters are easy to derive from observations and model calculations and are therefore well suited to systematic studies of the dust scattering in circumstellar disks.

Key words. stars: pre-main sequence – planetary systems: debris disks – planetary systems: protoplanetary disks – star: individual object: HR 4796A – Techniques: polarimetric

1. Introduction

Circumstellar disks reflect the light from the central star, and the produced scattered intensity and polarization contain a lot of information about the disk geometry and the scattering dust particles. The scattered light of disks is usually only a contribution of a few percent or less to the direct light from the central star and therefore requires observations with sufficiently high resolution and contrast to resolve the disk from the star. This was achieved in recent years for many circumstellar disks with adaptive optics (AO) systems at large telescopes using polarimetry, a powerful high-contrast technique, to disentangle the scattered and therefore polarized light of the disk from the direct and typically unpolarized light of the central star (e.g., Apai et al. 2004; Oppenheimer et al. 2008; Quanz et al. 2011; Hashimoto et al. 2011; Muto et al. 2012).

With AO systems, the observational point spread function (PSF) depends to a large extent on the atmospheric turbulence and is highly variable (e.g., Cantalloube et al. 2019). For this reason, the disks are often only detected in polarized light and it is not possible to disentangle the disk intensity signal from the strong, variable PSF of the central star (see e.g., Esposito et al. 2020). Therefore, analyses of the scattered light from the disk are often based on the differential polarization alone and only in favorable cases can one combine this with measurements of the disk intensity. For the data analysis, the observed polarization must first be corrected for instrumental polarization effects, and this is relatively difficult for complex AO systems (e.g., Schmid 2021, and references therein). For this reason, the first generation of AO systems with polarimetric mode provided useful qualitative polarimetric results but hardly any quantitative results.

This situation has changed with the new extreme AO systems GPI (Macintosh et al. 2014) and SPHERE (Beuzit et al. 2019), which, in addition to better image quality, also provide polarimetrically calibrated data for the circumstellar disk (Perrin et al. 2015; Schmid et al. 2018; de Boer et al. 2020; van Holstein et al. 2020). Thus, quantitative polarization measurements are now possible for many circumstellar disks. However, the technique is not yet well established, and detailed studies have only been made for a few bright, extended disks; for example for HR 4796A (Perrin et al. 2015; Milli et al. 2019; Arriaga et al. 2020), HIP 79977 (Engler et al. 2017), HD 34700A (Monnier et al. 2019), HD 169142 (Tschudi & Schmid 2021), and HD 142527 (Hunziker et al. 2021). There also exist a few polarimetric studies based on HST polarimetry, such as those for the disks of AU Mic (Graham et al. 2007) or AB Aur (Perrin et al. 2009). The large majority of polarimetric disk observations in the literature focus their analysis on the high-resolution disk geometry (e.g., Benisty et al. 2015; Garufi et al. 2016; Avenhaus et al. 2018), and therefore the measurements are not calibrated and polarimetric cancelation effects introduced by the limited spatial resolution are not taken into account. Even for the detailed polarimetric studies mentioned above, the derived photo-polarimetric parameters are relatively heterogeneous. Convolution effects are only sometimes taken into account, and measurements are given as observed maps, azimuthal or radial profiles, or as dust parameters of a well-fitting disk model. This makes a comparison of results between different studies difficult and inaccurate, in particular because measuring uncertainties and model ambiguities are rarely discussed in detail.

Therefore, this paper introduces Stokes Q and U quadrant polarization parameters, which are simple to derive but still well defined, and facilitate systematic, quantitative studies of larger samples of circumstellar disks in order to make polarimetric measurements more valuable for our understanding of the physical properties of the scattering dust. Quantitative polarimetry of disks might be very useful to clarify whether dust properties are different or similar for systems with different morphology, age, level of illumination, or dust composition. The quadrant polarization parameters should also be useful for model simulations describing the appearance of a given disk for different inclinations so that intrinsic properties can be disentangled from the effects of a particular disk inclination. The same parameters can also be used to quantify the impact of the convolution of the intrinsic disk signal or of simulated images with instrumental PSF profiles to correct the observable polarization of small and large disks for the effects of smearing and polarimetric degradation (Schmid et al. 2006).

Using Stokes Q and U quadrant parameters for the description of the polarization of disks is a new approach and to the best of our knowledge this is the first publication using this type of analysis. These quadrant polarization parameters are introduced in Sect. 2 using the published data of Milli et al. (2019) for the bright debris disk HR 4796A as an example. The interpretation of the measured values is illustrated with corresponding model calculations for optically thin debris disks, which are described in Sect. 3. The models are similar to the classical simulation for the scattered intensity of debris disks of Artymowicz et al. (1989) and Kalas & Jewitt (1996), but they also consider the scattering polarization as in the models of Graham et al. (2007) and Engler et al. (2017). It is shown in Sect. 4 that the relative quadrant polarization values for optically thin, axisymmetric (and flat) debris disks are independent of the radial dust distribution and they depend only on the disk inclination i and the shape of the polarized scattering phase function $f_\phi(\theta)$. Therefore,

in Sect. 5 we construct simple diagnostic diagrams for quadrant polarization parameters which constrain the $f_\phi(\theta)$ function for a given i , or directly yield the scattering asymmetry parameter g if we adopt a Henyey-Greenstein scattering function for the dust. The diagnostic diagrams are applied to the quadrant polarization measurements of HR 4796A and the obtained results are compared with the detailed, model-free phase-curve extraction of Milli et al. (2019). Finally, in Sect. 6 we discuss the potential and limitations of the quadrant polarization parameters for the analysis of disk observations and model simulations in a broader context.

2. Quadrant polarization parameters for disks

2.1. Polarization parameters in sky coordinates

Polarimetric imaging of stellar systems with circumstellar disks provides typically sky images for the intensity $I_{\text{obs}}(\alpha, \delta)$ and the Stokes linear polarization parameters $Q_{\text{obs}}(\alpha, \delta)$ and $U_{\text{obs}}(\alpha, \delta)$. For dust scattering, the circular polarization is expected to be much smaller than the linear polarization and is usually not measured; it is therefore neglected in this work. Q and U are differential quantities for the linear polarization components

$$Q = I_0 - I_{90} \quad \text{and} \quad U = I_{45} - I_{135}, \quad (1)$$

which can also be expressed as polarization flux $P = p \times I = (Q^2 + U^2)^{1/2}$ and polarization position angle $\theta_p = 0.5 \text{atan2}(U, Q)^1$. The polarized flux $p \times I$ is by definition a positive quantity, which, for noisy Q or U imaging data, suffers from a significant bias effect (Simmons & Stewart 1985).

The azimuthal Stokes parameter Q_ϕ can be used as an alternative for P for circumstellar disks. Q_ϕ measures polarization in the azimuthal direction with respect to the central star (α_0, δ_0) and U_ϕ in a direction rotated by 45° with respect to azimuthal. Circumstellar dust, which scatters light from the central star, mostly produces polarization with azimuthal orientations $\theta_p \approx \phi_{\alpha\delta} + 90^\circ$, while U_ϕ is almost zero. Therefore, Q_ϕ can be considered as a good approximation for the polarized flux of the scattered radiation from circumstellar disks $p \times I = (Q_\phi^2 + U_\phi^2)^{1/2} \approx Q_\phi$, and this approximation also avoids the noise bias problem (Schmid et al. 2006). For the model calculations of optically thin disks presented in this work, there is strictly $p \times I = Q_\phi$, while small signals $U_\phi < 0.05 Q_\phi$ can be produced by multiple scattering in optically thick disks (Canovas et al. 2015) or disks with aligned aspherical scattering particles. The U_ϕ signal is often much larger, that is, $U_\phi \gtrsim 0.1 Q_\phi$, in observations because of the PSF convolution problem for poorly resolved disks and polarimetric calibration errors. Both effects should be taken into account and corrected for the polarimetric measurements of disks. The azimuthal Stokes parameters are defined by

$$Q_\phi(\alpha, \delta) = -Q(\alpha, \delta) \cos(2\phi_{\alpha\delta}) - U(\alpha, \delta) \sin(2\phi_{\alpha\delta}), \quad (2)$$

$$U_\phi(\alpha, \delta) = +Q(\alpha, \delta) \sin(2\phi_{\alpha\delta}) - U(\alpha, \delta) \cos(2\phi_{\alpha\delta}), \quad (3)$$

with

$$\phi_{\alpha\delta} = \text{atan2}((\delta - \delta_0), (\alpha - \alpha_0)), \quad (4)$$

according to the description of Schmid et al. (2006) for the radial Stokes parameters Q_r, U_r , and using $Q_\phi = -Q_r$ and $U_\phi = -U_r$.

¹ defined as in the FORTRAN function $\text{atan2}(y, x)$ for Cartesian to polar coordinate conversions

2.2. Disk integrated polarization parameters

Quantitative measurements of the scattered radiation from circumstellar disks were obtained in the past with aperture polarimetry, which provided the disk-integrated Stokes parameters \overline{Q} , \overline{U} or the polarized flux $\overline{P} = (\overline{Q}^2 + \overline{U}^2)^{1/2}$ usually expressed as fractional polarization relative to the system-integrated intensity $\overline{Q}/\overline{I}_{\text{tot}}$, $\overline{U}/\overline{I}_{\text{tot}}$, or $\overline{P}/\overline{I}_{\text{tot}}$ and the averaged polarization position angle $\langle\theta_p\rangle = 0.5 \text{atan}2(\overline{U}, \overline{Q})$ (e.g., Bastien 1982; Yudin & Evans 1998). This polarization signal can be attributed to the scattered light from the disk if the star produces no polarization and if the interstellar polarization can be neglected, or if these contributions can be corrected. Usually, the disk intensity $\overline{I} = \overline{I}_{\text{tot}} - \overline{I}_{\text{star}}$ cannot be distinguished from the stellar intensity with aperture polarimetry, apart from a few exceptional cases, such as that of β Pic.

Aperture polarimetry provides only the net scattering polarization, but misses potentially strong positive and negative polarization components $+Q$, $-Q$ and $+U$, $-U$ which cancel each other in unresolved observations. Therefore, \overline{Q} and \overline{U} , or \overline{P} and $\langle\theta_p\rangle$ provide only one value and one direction for circumstellar disks, which agglomerate all possible types of deviations from axisymmetry of the scattering polarization of a circumstellar disk.

Disk-resolved polarimetric imaging avoids or strongly reduces the destructive cancellation effect and provides therefore much more information about the scattering polarization of disks. The most basic polarization parameter for the characterization of a resolved disk is the disk integrated azimuthal polarization \overline{Q}_ϕ which can be considered as equivalent to the polarized flux for resolved observations \overline{P}^2 . The integrated polarized flux \overline{Q}_ϕ depends on the spatial resolution of the data; this aspect is not considered in this work because for well-resolved disks, like that of HR 4796A, the effect of limited spatial resolution is small and can be corrected with modeling of the instrumental smearing.

If the disk intensity \overline{I} is measurable, one can also determine the disk-averaged fractional polarization $\langle p_\phi\rangle = \overline{Q}_\phi/\overline{I}$. Unfortunately, it is still often very difficult to measure the disk intensity $I(\alpha, \delta)$ with AO-observations because the signal cannot be separated from the intensity of the variable point spread function $I_{\text{star}}(\alpha, \delta)$ of the much brighter central star. In these cases, the fractional polarization can only be expressed relative to the total system intensity $\langle p_{\phi, \text{tot}}\rangle = \overline{Q}_\phi/\overline{I}_{\text{tot}}$. Integrated or averaged quantities are well defined but not well suited to characterizing the polarimetric features and the azimuthal dependence of the polarization for circumstellar disks. Therefore, we introduce new polarization parameters to quantify the individual positive and negative polarimetric components $+Q$, $-Q$ and $+U$, $-U$ of spatially resolved disk observations and models.

2.3. Quadrant polarization parameters in disk coordinates

For polarimetric imaging of circumstellar disks, the geometric orientation of the disk and the Stokes Q and U parameters are often described in sky coordinates. This is inconvenient for the characterization of the intrinsic scattering geometry of the disk and therefore we define new polarization parameters Q_d and U_d in the disk coordinate system (x, y) , where the central star is at $x_0 = 0, y_0 = 0$ and the x and y are aligned with the major and

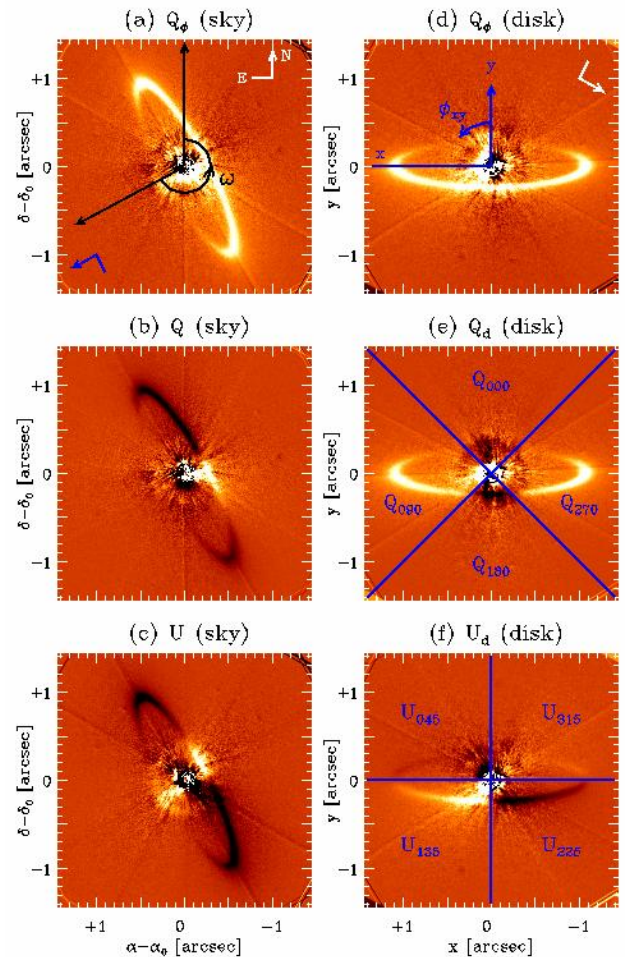


Fig. 1. Illustration of the definition of the quadrant polarization parameters (panels e and f) for the observations of the debris disk around HR 4796A from Milli et al. (2019). Left: Azimuthal polarization Q_ϕ and Stokes Q and U in relative α, δ -sky coordinates; Right: Q_ϕ , Q_d , and U_d in x, y -disk coordinates.

minor axis of the projected disk, respectively. The positive x -axis is pointing left to ease the comparison with observations in relative sky coordinates $\alpha - \alpha_0$ and $\delta - \delta_0$ and to get the same convention for the Q_d and U_d orientations in x, y and sky images. Thus, the relative $\alpha - \alpha_0, \delta - \delta_0$ sky coordinates of the observed images I, Q_ϕ, Q , and U must be rotated according to

$$x = (\alpha - \alpha_0) \cos \omega + (\delta - \delta_0) \sin \omega, \quad (5)$$

$$y = (\delta - \delta_0) \cos \omega - (\alpha - \alpha_0) \sin \omega. \quad (6)$$

as shown in Fig. 1 for the imaging polarimetry of HR 4796A using $\omega = 242^\circ$ (-118°). We use the convention that ω aligns the more distant semi-minor axis of the projected disk with the positive (upward) y -axis.

Also, the Stokes parameters for the linear polarization must be rotated from the Q, U sky system to the Q_d, U_d disk system using the geometrically rotated (x, y) -frames

$$Q_d(x, y) = Q(x, y) \cos(2\omega) + U(x, y) \sin(2\omega), \quad (7)$$

$$U_d(x, y) = U(x, y) \cos(2\omega) - Q(x, y) \sin(2\omega). \quad (8)$$

We define for the $Q_d(x, y)$ and $U_d(x, y)$ polarization images the quadrant parameters $Q_{000}, Q_{090}, Q_{180}$, and Q_{270} for Stokes Q_d and $U_{045}, U_{135}, U_{225}$, and U_{315} for Stokes U_d , which are obtained by integrating the Stokes Q_d or U_d disk polarization signal in the corresponding quadrants as shown in Fig. 1 (e) and

² We distinguish between the polarized flux derived from resolved observations \overline{P} and unresolved aperture polarimetry \overline{P} .

(f). This selection of polarization parameters is of course motivated by the natural Q and U quadrant patterns for circumstellar scattering where the signal in a given quadrant typically has the same sign everywhere and is almost zero at the borders of the defined integration region. This is strictly the case for all the model calculations for optically thin debris disks presented in this work and the same type of quadrant pattern is also predominant for the scattering polarization of proto-planetary disks. Multiple scattering and grain alignment effects can introduce deviations from a “clean” quadrant polarization pattern which may be measurable in high-quality observations (Canovas et al. 2015). However, the smearing and polarization cancellation effects introduced by the limited spatial resolution are typically much more important in affecting the quadrant pattern. For poor spatial resolution or very small disks, the quadrant pattern disappears (Schmid et al. 2006) or is strongly disturbed for asymmetric systems (Heikamp & Keller 2019).

Eight quadrant polarization values seems to be a useful number for the characterization of the azimuthal distribution of the polarization signal of disks. The parameters provide some redundancy to check and verify systematic effects, or to allow alternative disk characterizations if one parameter is not easily measurable or is affected by a special disk feature. Let us consider the redundancy in the context of the geometrical symmetry of disks and the dust scattering asymmetry.

For an inclined, but intrinsically axisymmetric disk, the Stokes Q_d quadrants have the symmetry

$$Q_{090} = Q_{270}, \quad (9)$$

and the Stokes U_d quadrants have the anti-symmetries

$$U_{045} = -U_{315} \quad \text{and} \quad U_{135} = -U_{225}. \quad (10)$$

Special cases generate additional equalities; for example the models with isotropic scattering (see Fig. 5) have a front-back symmetry and therefore there is also $Q_{000} = Q_{180}$ and $U_{045} = -U_{135} = U_{225} = -U_{315}$. For an axisymmetric disk seen pole-on, all quadrant parameters have the same absolute value. If a disk deviates from an intrinsically symmetric geometry, for example a brighter $+x$ side, then this would result in $|Q_{090}| > |Q_{270}|$ for Stokes Q_d and $|U_{045}| > |U_{315}|$ or $|U_{135}| > |U_{225}|$ for Stokes U_d .

Dust, which is predominantly forward scattering, produces more signal for front side polarization quadrants compared to the backside quadrants and this is equivalent to $|Q_{180}| > |Q_{000}|$ or $|U_{135}| > |U_{045}|$ and $|U_{225}| > |U_{315}|$. Properties that can be deduced from parameter ratios derived from the same data set are important because this reduces the impact of at least some systematic uncertainties in the measurements.

The quadrant parameters are also linked to the integrated polarization parameters \overline{Q}_ϕ , \overline{Q}_d , and \overline{U}_d . For the sum of all four Stokes Q_d and Stokes U_d quadrants, there is

$$\Sigma Q_{xxx} = \overline{Q}_d \quad \text{and} \quad \Sigma U_{xxx} = \overline{U}_d. \quad (11)$$

For pole-on systems, there is $\overline{Q}_d = \overline{U}_d = 0$, because of the symmetric cancellation of positive and negative quadrants and intrinsically axis-symmetric systems have $\overline{U}_d = 0$ for all disk inclinations because of the left-right antisymmetry. Axisymmetric but inclined systems have $\overline{Q}_d \neq 0$ in general. For disks with larger inclination i , a smaller fraction of the disk is “located” in the quadrants Q_{000} and Q_{180} and a larger fraction is located in Q_{090} and Q_{270} near the major axis because of the disk projection. Edge-on disks are almost only located in the quadrants

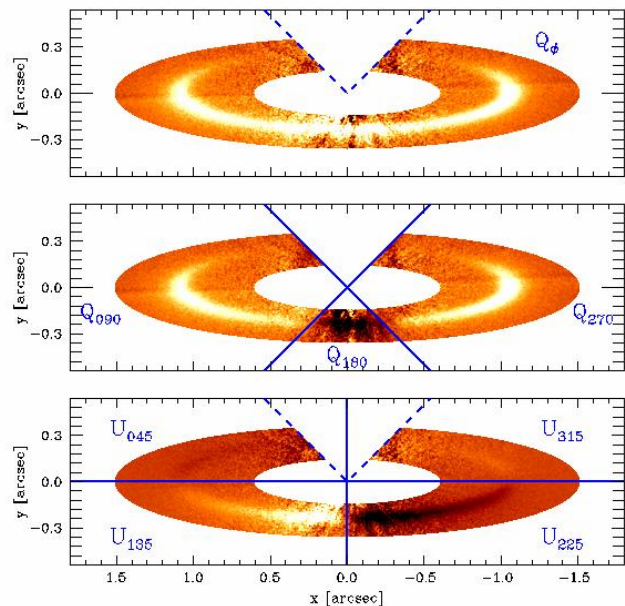


Fig. 2. Apertures used for the measurements of the integrated azimuthal polarization \overline{Q}_ϕ (top), the Stokes Q_d quadrants (middle), and the Stokes U_d quadrants (bottom) for HR 4796A.

Q_{090} and Q_{270} and quadrant sums approach $Q_{000} + Q_{180} \rightarrow 0$ and $Q_{090} + Q_{270} \rightarrow \overline{Q}_d$ for $i \rightarrow 90^\circ$.

For the sums of the four absolute quadrant parameters for Stokes Q_d , there is of course

$$\Sigma |Q_{xxx}| > \Sigma Q_{xxx} \quad \text{and} \quad \Sigma |Q_{xxx}| < \overline{Q}_\phi, \quad (12)$$

and the equivalent exists for sums of the Stokes U_d quadrants. For a pole-on view, the system is axisymmetric with respect to the line of sight and there is

$$\Sigma |Q_{xxx}| = \Sigma |U_{xxx}| = \frac{2}{\pi} \overline{Q}_\phi, \quad (13)$$

where each quadrant has the same absolute value of $\overline{Q}_\phi/2\pi = 0.159 \overline{Q}_\phi$. These sums will converge for edge-on disks $i = 90^\circ$ to $\Sigma |Q_{xxx}| \rightarrow \overline{Q}_\phi$ for Stokes Q_d and to $\Sigma |U_{xxx}| \rightarrow 0$ for Stokes U_d .

2.4. Quadrant polarization parameters for HR 4796A

We use the high-quality differential polarimetric imaging (DPI) of the bright debris disk HR 4796A from Milli et al. (2019) shown in Fig. 1 as an example for the measurement of the quadrant polarization parameters. The data were taken with the SPHERE/ZIMPOL instrument (Beuzit et al. 2019; Schmid et al. 2018) in the very broad band (VBB) filter with the central wavelength $\lambda_c = 735$ nm and full width of $\Delta\lambda = 290$ nm.

These data provide “only” the differential Stokes $Q(x, y)$ and $U(x, y)$ signals or the corresponding azimuthal quantities $Q_\phi(x, y)$ and $U_\phi(x, y)$, but no intensity signal because it is difficult with AO-observations to separate the disk intensity from the variable intensity PSF of the much brighter central star. The scattered light of the disk around HR 4796A was previously detected in polarization and intensity with AO systems in the near-IR (e.g., Milli et al. 2017; Chen et al. 2020; Arriaga et al. 2020), and in intensity in the visual with HST (e.g., Schneider et al. 2009).

Quadrant polarization parameters Q_{xxx} and U_{xxx} for HR 4796A derived from the data shown in Fig. 1(e) and (f) are given in Table 1 as relative values using the integrated polarized flux \overline{Q}_ϕ as reference. The quadrant values were obtained by integrating the counts in the annular apertures sections as illustrated in Fig. 2, which avoid the high noise regions from the PSF peak in the center. The uncertainties indicated in Table 1 account for the image noise, but do not account for systematic effects related to the selected aperture geometry or polarimetric calibration uncertainties. The noise errors are particularly large for the quadrants Q_{000} and Q_{180} because of the small separation of these disk sections from the bright star and additional negative noise spikes which are particularly strong for the Q_{000} quadrant. Because of this noise, the formal integration gives $Q_{000}/\overline{Q}_\phi = -0.04$. From the decreasing trend of the signal in for example Q_ϕ towards the back side of the disk and the measured disk signals of about 0.03 for $U_{045}/\overline{Q}_\phi$ or $U_{315}/\overline{Q}_\phi$, an absolute signal of less than $|Q_{000}|/\overline{Q}_\phi < 0.01$ is expected for a smooth dust distribution in the ring and any reasonable assumptions for the dust scattering. Therefore, we do not consider the noisy Q_{000} -measurement in the quadrant sums ΣQ_{xxx} . The noise in the Q_{180} -quadrant is also significantly enhanced when compared to other quadrants despite the relatively strong signal and the small integration area. A detailed analysis of the noise pattern might improve the measuring accuracy, but this is beyond the scope of this paper.

Because of the noise, the apertures for Q_ϕ and the quadrants U_{045} and U_{135} were restricted to avoid the noisy and essentially signal-free region around $\phi_{xy} \approx 0^\circ$. One should note that uncertainties for the quadrant measurements, for example for Q_{180} , also affect the Q_ϕ value and a dominant noise feature therefore has an enhanced impact on relative parameters such as $Q_{xxx}/\overline{Q}_\phi$, which include the disk integrated azimuthal polarization \overline{Q}_ϕ . These are typical problems for high-contrast observations of inclined disks and it can be very useful to select only high-signal-to-noise quadrant values for the characterization of the azimuthal dependence of the disk polarization.

Asymmetries between the left and right or the positive and negative sides of the x -axis can be deduced from the absolute quadrant parameters $|Q_{090}|$ and $|Q_{270}|$, $|U_{045}|$ and $|U_{315}|$, and $|U_{135}|$ and $|U_{225}|$. Table 1 gives relative left–right brightness differences Δ_{bbb}^{aaa} calculated according to

$$\Delta_{270}^{090} = \frac{|Q_{090}| - |Q_{270}|}{|Q_{090}| + |Q_{270}|} \quad (14)$$

for Stokes Q_d parameters and equivalent for Δ_{315}^{045} and Δ_{225}^{135} for Stokes U_d .

The asymmetry values Δ_{270}^{090} and Δ_{225}^{135} both yield more flux on the left side of the (x, y) -plane, which is the SW-side for the HR 4796A disk. This does not agree with previous determinations, including even the analysis of the same data by Milli et al. (2019) who measured more flux on the NE side. A more detailed investigation reveals that the peak surface brightness is indeed higher for the disk on the NE side and that the left–right asymmetry depends on the width of the annular apertures used for the flux extraction. If we integrate only a narrow annular region with a full width of $\Delta x = 0.1''$ at the location of the major axis then we also get more flux for the NE side or negative Δ_{270}^{090} -values of $-3 \pm 2\%$ but still less than the “negative” (SW-NE) asymmetry measured by Milli et al. (2019) for Q_ϕ or Schneider et al. (2018) for the intensity. We therefore conclude that there are subtle asymmetries at the level of $\Delta \approx 10\%$ present for the disk HR 4796A, which are positive for a wide flux extraction and negative for a narrow flux extraction. Measurement uncertainties in

Table 1. Measured relative quadrant polarization parameters for HR 4796A, deviations Δ (in %) from left–right symmetry and ratios Λ for back–front flux ratios.

Stokes Q_d quadrants		Stokes U_d quadrants	
relative quadrant polarization (errors: $\approx \pm 0.010$)			
$Q_{000}/\overline{Q}_\phi$	-0.04^a	$U_{045}/\overline{Q}_\phi$	-0.031
$Q_{090}/\overline{Q}_\phi$	$+0.385$	$U_{135}/\overline{Q}_\phi$	$+0.212$
$Q_{180}/\overline{Q}_\phi$	-0.076^b	$U_{225}/\overline{Q}_\phi$	-0.159
$Q_{270}/\overline{Q}_\phi$	$+0.343$	$U_{315}/\overline{Q}_\phi$	$+0.033$
quadrant sums (errors: $\approx \pm 0.030$)			
$\Sigma Q_{xxx}/\overline{Q}_\phi$	$+0.652^c$	$\Sigma U_{xxx}/\overline{Q}_\phi$	$+0.055$
$\Sigma Q_{xxx} /\overline{Q}_\phi$	0.804^c	$\Sigma U_{xxx} /\overline{Q}_\phi$	0.435
left–right asymmetry parameters			
Δ_{270}^{090}	$+6 \pm 2\%$	Δ_{225}^{135}	$+14 \pm 4\%$
		Δ_{315}^{045}	$-3 \pm 2\%$
back–front parameter ratios			
Λ_{180}^{000}	< 0.6	Λ_{135}^{045}	0.15 ± 0.07
		Λ_{225}^{315}	0.21 ± 0.09
special back–front parameter ratios			
$\Lambda_a = (Q_{090} + Q_{270})/(2 Q_{180})$			4.8 ± 0.7
$\Lambda_b = (Q_{090} + Q_{270})/(U_{135} + U_{225})$			2.0 ± 0.2

Notes. ^(a) strongly affected by noise, the expected signal is $|Q_{000}| < 0.01$; ^(b) errors: $\approx \pm 0.020$; ^(c) Q_{000} is not included in ΣQ_{xxx} .

the left–right differences are at the few percent level for bright quadrant pairs.

The back-side to front-side brightness contrast can be expressed with quadrant ratios such as

$$\Lambda_{180}^{000} = \frac{|Q_{000}|}{|Q_{180}|}, \text{ and } \Lambda_{135}^{045} = \frac{|U_{045}|}{|Q_{135}|}, \text{ or } \Lambda_{225}^{315} = \frac{|U_{315}|}{|U_{225}|}, \quad (15)$$

and their equivalents for other quadrant ratios. These ratios are small $\lesssim 0.5$ for HR 4796A which is indicative of dust with a strong forward scattering phase function. For isotropic scattering in an axisymmetric disk, the ratios would be $\Lambda_{180}^{000} = \Lambda_{135}^{045} = 1$ for all inclinations. Because the polarization flux in the backside quadrants is small, one can also assess the disk forward scattering with a comparison of the brighter Q_{090} and Q_{270} quadrants with the Stokes Q_d front quadrant Q_{180} or the Stokes U_d front quadrants U_{135} and U_{225} as given in Table 1.

As demonstrated in Table 1, the polarization quadrants provide a useful set of parameters for the quantitative characterization of the geometric distribution of the polarization signal in circumstellar disks. Comparisons with model calculations are required to assess the diagnostic power of the derived values for the determination of the scattering properties of the dust or for the interpretation of the strength of disk asymmetries.

3. Disk model calculations

The simple disk models presented in this work follow the basic calculations for the scattered intensity from debris disks (Artymowicz et al. 1989; Kalas & Jewitt 1996) and the scattering polarization (e.g., Bastien & Menard 1988; Whitney & Hartmann 1992; Graham et al. 2007; Engler et al. 2017) but focus on the azimuthal dependence of the scattering polarization and the determination of the quadrant polarization values.

The model disks are described by a dust-density distribution in cylindrical coordinates $\rho(r, \varphi_d, h)$ where r is the radius vector $r = (x_d^2 + y_d^2)^{-1/2}$ and φ_d the azimuthal angle in the disk plane³, where x_d coincides with x for the major axis of the projected, inclined disk. We consider in this work very simple, optically thin $\tau \ll 1$, axisymmetric models $\rho(r, h)$, where the dust scattering cross-section per unit mass σ_{sca} is independent of the location. The total dust scattering emissivity (integrated over all directions) $\epsilon(r, h)$ of a volume element is given by the stellar flux $F_\lambda(r, h) = L_\lambda / (4\pi(r^2 + h^2))$, the disk density $\rho(r, h)$, and σ_{sca} :

$$\epsilon(r, h) = \frac{L_\lambda}{4\pi(r^2 + h^2)} \rho(r, h) \sigma_{\text{sca}}. \quad (16)$$

The incident flux decreases as $F_\lambda \propto 1/R^2$ with $R^2 = r^2 + h^2$, because in our optically thin scattering model we neglect the extinction of stellar light by the dust and the addition of diffuse light produced by the scatterings in the disk.

The resulting images for the scattered light intensity $I(x, y)$ and the azimuthal polarization $Q_\phi(x, y)$ are obtained with a line of sight or z -axis integration of the scattering emissivity ϵ and the scattering phase functions $f_I(\theta_{\text{xyz}}, g)$ for the intensity

$$I(x, y) = \int \epsilon(x, y, z) f_I(\theta_{\text{xyz}}, g) dz, \quad (17)$$

and $f_\phi(\theta_{\text{xyz}}, g, p_{\text{max}})$ for the polarized intensity

$$Q_\phi(x, y) = \int \epsilon(x, y, z) f_\phi(\theta_{\text{xyz}}, g, p_{\text{max}}) dz. \quad (18)$$

The transformations from the disk coordinate system (r, φ_d, h) with $x_d = r \sin \varphi_d$ and $y_d = r \cos \varphi_d$ to the sky coordinate system (x, y, z) is given by $x = x_d$, $y = y_d \cos i + h \sin i$ and $z = y_d \sin i - h \cos i$ where i is the disk inclination. This also defines the scattering angle θ_{xyz} and the radial separation to the central star R_{xyz} for each point (x, y, z) .

3.1. Scattering phase functions

The scattering phase function $f_I(\theta, g)$ for the intensity is described by the Henyey-Greenstein function or HG-function (Henyey & Greenstein 1941), where θ is the angle of deflection

$$f_I(\theta, g) = \frac{1}{4\pi} \frac{1 - g^2}{(1 + g^2 - 2g \cos \theta)^{3/2}}. \quad (19)$$

The asymmetry parameter g is defined between -1 and $+1$ and backward scattering dominates for negative g , forward scattering dominates for positive g , while the scattering is isotropic for $g = 0$.

The scattering phase function $f_\phi(\theta, g, p_{\text{max}})$ for the polarized flux adopts the same angle dependence for the fractional polarization as Rayleigh scattering, but with the scale factor $p_{\text{max}} \leq 1$ for the maximum polarization at $\theta = 90^\circ$. This description is often used (e.g., Graham et al. 2007; Buenzli & Schmid 2009; Engler et al. 2017) as a simple approximation for a Rayleigh scattering-like angle dependence but reduced polarization induced by dust particles (e.g., Kolokolova & Kimura 2010; Min et al. 2016; Tazaki et al. 2019).

The angle dependence of the fractional polarization of the scattered light is

$$p_{\text{sca}}(\theta, p_{\text{max}}) = \frac{Q_{\text{sca}}}{I_{\text{sca}}} = p_{\text{max}} \frac{1 - \cos^2 \theta}{1 + \cos^2 \theta}. \quad (20)$$

³ the azimuthal angle φ_d defined in the disk plane is different from the azimuthal angle ϕ_{xy} , which is defined in the sky plane.

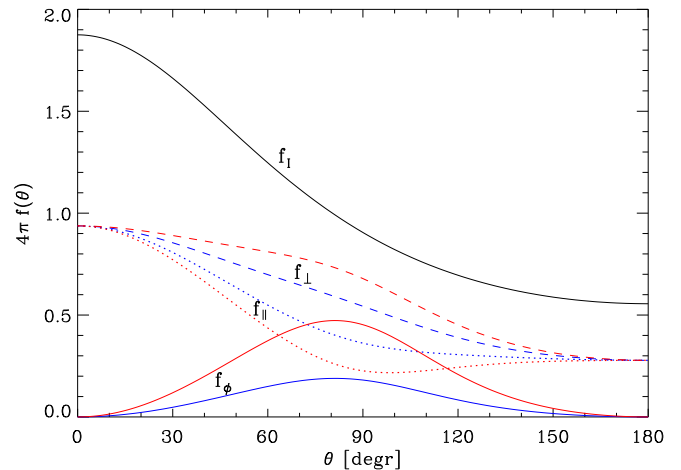


Fig. 3. Scattering phase functions for the HG asymmetry parameter $g = 0.2$ for the total intensity $4\pi f_I(\theta)$ (black), for the polarized intensities $4\pi f_\perp(\theta)$ (dashed) and $4\pi f_\parallel(\theta)$ (dotted), for the two values $p_{\text{max}} = 0.5$ (red) and 0.2 (blue), and the corresponding scattering phase functions for the polarized flux $4\pi f_\phi(\theta)$ (full, colored lines).

The scattered intensity I_{sca} can be split into the perpendicular I_\perp and parallel I_\parallel polarization components with respect to the scattering plane, so that $I_{\text{sca}} = I_\perp + I_\parallel$, $Q_{\text{sca}} = I_\perp - I_\parallel$ and $I_\perp = (I_{\text{sca}} + Q_{\text{sca}})/2$, $I_\parallel = (I_{\text{sca}} - Q_{\text{sca}})/2$. Together with p_{sca} , this yields

$$I_\perp(p_{\text{max}}, \theta) = I_{\text{sca}} \cdot \left[0.5 + p_{\text{max}} \left(\frac{1}{1 + \cos^2 \theta} - 0.5 \right) \right], \quad (21)$$

$$I_\parallel(p_{\text{max}}, \theta) = I_{\text{sca}} \cdot \left[0.5 + p_{\text{max}} \left(\frac{\cos^2 \theta}{1 + \cos^2 \theta} - 0.5 \right) \right], \quad (22)$$

or, expressed as scattering phase functions, $f_\perp = f_I k_\perp(\theta, p_{\text{max}})$ and $f_\parallel = f_I k_\parallel(\theta, p_{\text{max}})$, where k_\perp and k_\parallel are the expressions in the square brackets and $p_{\text{sca}} = k_\perp - k_\parallel$.

The scattering plane in a projected image of a circumstellar disk has always a radial orientation with respect to the central star. Therefore the induced scattering polarization Q_{sca} , which is perpendicular to the scattering plane, translates into an azimuthal polarization Q_ϕ for the projected disk map. The scattering phase functions are related by

$$f_\phi(\theta, g, p_{\text{max}}) = p_{\text{max}} f_\phi^n(\theta, g) = f_I(\theta, g) p_{\text{sca}}(\theta, p_{\text{max}}), \quad (23)$$

where f_ϕ can be separated into a normalized part f_ϕ^n for $p_{\text{max}} = 1$ and the scale factor p_{max} .

Figure 3 illustrates the scattering phase functions for $g = 0.2$ for the total intensity f_I and the corresponding polarization components f_\perp and f_\parallel for $p_{\text{max}} = 0.5$ and 0.2 . The differential phase function $f_\phi = f_\perp - f_\parallel$ has the same θ -dependence $f_\phi^n(\theta, g)$ for both cases, and only the amplitude scales with p_{max} . In this formalism, the total intensity phase function $f_I(g, \theta)$ does not depend on the adopted polarization parameter p_{max} . Expected values for approximating dust scattering with HG scattering functions are $p_{\text{max}} \approx 0.05 - 0.8$, but we often set this scale factor in this work to $p_{\text{max}} = 1$ because this allows us to plot the intensity and polarization on the same scale. A value $p_{\text{max}} = 1$ applies for Rayleigh scattering but the HG-function with $g = 0$ (isotropic scattering) differs from the Rayleigh scattering function for the intensity⁴. Hereafter, $f_\phi(\theta, g, p_{\text{max}})$ and $f_\phi^n(\theta, g)$ are also referred to as the HG_{pol} -function and normalized HG_{pol} -function, respectively.

⁴ Rayleigh scattering produces more forward and backward scattering when compared to isotropic scattering

The polarimetric scattering phase function for the azimuthal Stokes parameters f_ϕ can be converted into phase functions f_Q and f_U for the Stokes Q_d and U_d parameters

$$f_Q(\theta_{xy}, g, p_{\max}) = -f_\phi(\theta_{xy}, g, p_{\max}) \cos(2\phi_{xy}), \quad (24)$$

$$f_U(\theta_{xy}, g, p_{\max}) = -f_\phi(\theta_{xy}, g, p_{\max}) \sin(2\phi_{xy}), \quad (25)$$

where $\phi_{xy} = \text{atan2}(y, x)$ is the azimuthal angle in the sky coordinates aligned with the disk as illustrated in Fig. 1. These simple relations are valid in our optical thin (single scattering) models because $U_\phi(x, y) = 0$ and the Stokes $Q_d(x, y)$ and $U_d(x, y)$ model images can then be calculated as in Q_ϕ in Eq. 18 but using the phase functions for f_Q and f_U .

3.2. Flat disk models and azimuthal phase functions

The calculations for the scattered flux $I(x, y)$ and polarization $Q_\phi(x, y)$ with Eqs. 17 and 18 are strongly simplified for a flat disk because the integrations for a given x - y coordinate along the z -coordinate can be replaced by single values for the separation r_{xy} from the star, for the scattering emissivity $\epsilon(r_{xy})$, and for the scattering angle θ_{xy} . The volume density ρ must be replaced by a vertical surface density $\Sigma(r)$ or a line-of-sight surface density $\Sigma(r)/\cos i$. Of course, the scattering in the disk plane must still be treated as in an optically thin disk,

$$\tau(r) = \int_0^r \kappa_\Sigma \Sigma(r) dr \ll 1, \quad (26)$$

where $\kappa_\Sigma = a_\Sigma + \sigma_\Sigma$ is the disk extinction coefficient composed of the contributions from absorption a_Σ and scattering σ_Σ .

3.2.1. Projected flat disk image

The scattered intensity and polarization for a flat disk are given by

$$I(x, y) = \epsilon(r_{xy}) f_I(\theta_{xy}, g), \quad (27)$$

$$Q_\phi(x, y) = \epsilon(r_{xy}) f_\phi(\theta_{xy}, g, p_{\max}), \quad (28)$$

and similar for the Stokes $Q_d(x, y)$ and $U_d(x, y)$ using the phase function from Eqs. 24 and 25. The scattering emissivity

$$\epsilon(r_{xy}) = \frac{L_\lambda}{4\pi r_{xy}^2} \sigma_\Sigma \frac{\Sigma(r_{xy})}{\cos i} \quad (29)$$

is proportional to the line-of-sight surface density $\Sigma(r_{xy})/\cos i$, which considers the disk inclination, and where $r_{xy}^2 = x^2 + (y/\cos i)^2$ and $\theta_{xy} = \text{acos}(-z_{xy}/r_{xy}) = \text{acos}(-y \tan i/r_{xy})$, because $y = y_d \cos i$ and $z_{xy} = y_d \sin i$.

In these equations for $I(x, y)$, $Q_\phi(x, y)$, $Q_d(x, y)$, and $U_d(x, y)$, the radial dependence of the scattering emissivity $\epsilon(r_{xy})$ is separated from the azimuthal dependence described by the scattering phase functions $f_I(\theta_{xy})$, $f_\phi(\theta_{xy})$, $f_Q(\theta_{xy})$, and $f_U(\theta_{xy})$. This is very favorable for the introduced quadrant parameters, which describe the polarization of the scattered light of disks with an azimuthal splitting of the signal $Q_d(x, y) \rightarrow Q_{000}, Q_{090}, Q_{180}, Q_{270}$ and $U_d(x, y) \rightarrow U_{045}, U_{135}, U_{225}, U_{315}$ by integrating the polarization in the corresponding quadrants outlined by the black lines in the Q_d and U_d panels of Figs. 4 and 5.

Disk images for $I(x, y)$, $Q_d(x, y)$, $U_d(x, y)$, and $Q_\phi(x, y)$ for flat disk models are shown in Fig. 4 for the asymmetry parameter $g = 0.3$, the scale factor $p_{\max} = 1$, and three different inclinations

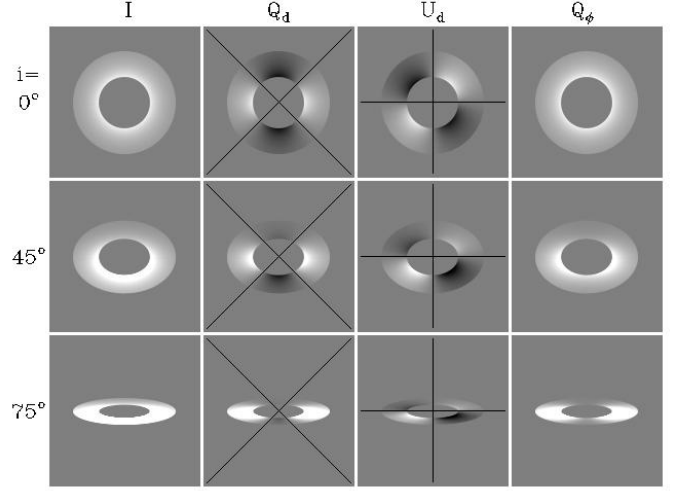


Fig. 4. I -, Q_d -, U_d - and Q_ϕ -images for a flat disk with $g = 0.3$, $p_{\max} = 1$, and for inclinations $i = 0^\circ$, $i = 45^\circ$, and 75° . The same gray scale from $+a$ (white) to $-a$ (black) is used for all panels. The black lines in the Q_d and U_d panels indicate the polarization quadrants.

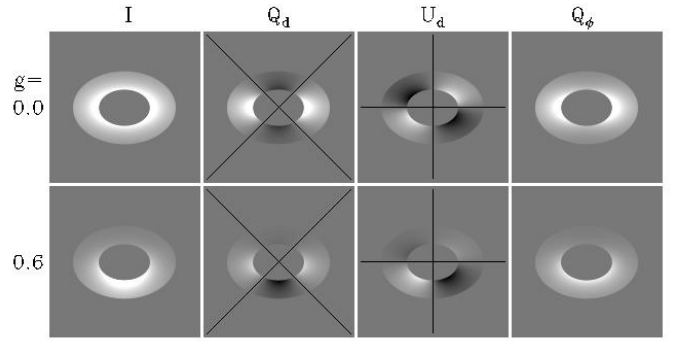


Fig. 5. I -, Q_d -, U_d - and Q_ϕ -images for flat disks with $i = 45^\circ$, $p_{\max} = 1$, and for scattering asymmetry parameter $g = 0.0$ and 0.6 . The same gray scale from $+a$ (white) to $-a$ (black) is used for all panels.

$i = 0^\circ$, 45° , and 75° . For the radial surface scattering emissivity, a radial dependence $\epsilon(r) \propto 1/r$ is adopted extending from an inner radius r_1 to the outer radius $r_2 = 2r_1$. Along the x -axis, the scattering angle is always $\theta_{xy} = 90^\circ$ and the surface brightness increases for higher inclinations as in the inclined surface emissivity $\propto 1/\cos i$.

The scattering asymmetry parameter g is relatively small and therefore the front-back brightness differences are not strong in Fig. 4. The forward scattering effect is much clearer in Fig. 5, where two disks are plotted with the same i and $\epsilon(r)$, but for isotropic scattering $g = 0$ and strong forward scattering $g = 0.6$.

For the disks shown in Figs. 4 and 5, the absolute signal drops in the radial direction for all azimuthal angles $\phi_{xy} = \text{atan2}(x, y)$ by exactly a factor of two from the inner edge $(r_1)_{xy}$ to the outer edge $(r_2)_{xy}$ according to the adopted radial dependence of the scattering emissivity $\epsilon(r) \propto 1/r$. This is equivalent to the statement that the (relative) azimuthal dependence along the ellipse r_{xy} describing a ring in the inclined disk is the same for all separations in a given disk image $I(r_{xy}, \phi_d)$, $Q_\phi(r_{xy}, \phi_d)$, $Q_d(r_{xy}, \phi_d)$, or $U_d(r_{xy}, \phi_d)$. This is also valid if the azimuthal an-

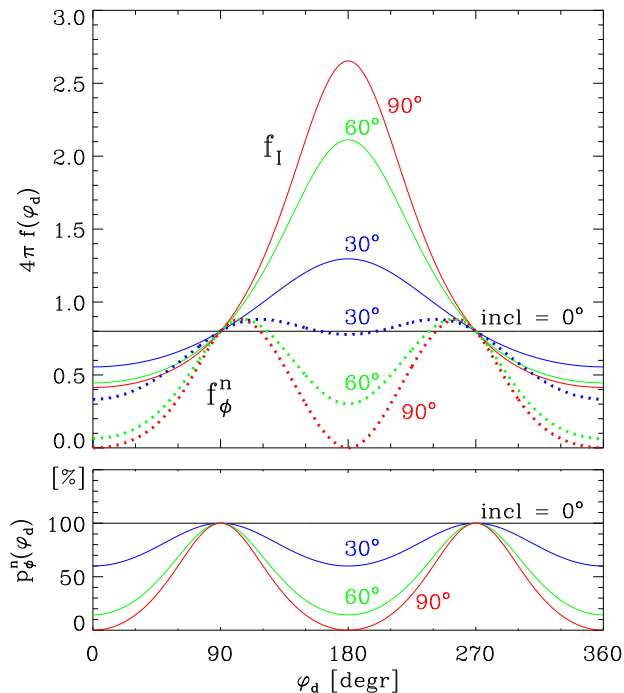


Fig. 6. Upper panel: Azimuthal dependence of the disk scattering phase function for the intensity $4\pi f_I(\varphi_d, i, g)$ and the normalized ($p_{\max} = 1$) polarized intensity $4\pi f_\phi^n(\varphi_d, i, g)$ for disks with scattering asymmetry parameter $g = 0.3$ and inclinations $i = 0^\circ, 30^\circ, 60^\circ,$ and 90° . Lower panel: Normalized fractional polarization $p_\phi^n(\varphi_d, i) = f_\phi^n/f_I$ for the same inclinations; p_ϕ^n does not depend on the g -parameters.

gle φ_d for the disk plane is replaced by the on-sky azimuthal angle ϕ .

Therefore, it is possible to determine the azimuthal dependence of the scattered light in a very simple way using azimuthal phase functions defined in the disk plane, without considering the radial distribution of the scattering emissivity.

3.2.2. Scattering phase functions for the disk azimuth angle

The azimuthal dependence of the scattered light can be calculated easily for flat, rotationally symmetric, and optically thin disks as a function of the azimuthal angle φ_d in the disk plane. For this, we have to express the scattering angle θ as a function of φ_d and the disk inclination i according to

$$\theta_{\varphi,i} = \theta(\varphi_d, i) = \arccos(\cos \varphi_d \cdot (-\sin i)), \quad (30)$$

where $\varphi_d = 0$ for the far-side semi-minor axis of the projected disk.

The dependence of the scattered intensity and polarization flux with disk azimuthal angle φ_d follows directly from the scattering phase functions f_I and f_ϕ and the change of the scattering angle θ as a function of φ_d and i

$$f_I(\varphi_d, i, g) = f_I(\theta_{\varphi,i}, g), \quad (31)$$

$$f_\phi(\varphi_d, i, g, p_{\max}) = p_{\max} f_\phi^n(\theta_{\varphi,i}, g) = f_\phi^n(\theta_{\varphi,i}, g, p_{\max}). \quad (32)$$

Figure 6 shows the azimuthal scattering functions $4\pi f_I(\varphi_d, i, g)$ for the intensity and $4\pi f_\phi^n(\varphi_d, i, g)$ for the polarized flux for $g = 0.3$ and for different inclinations. The factor 4π normalizes the isotropic scattering case $4\pi f_I(\varphi_d, i, g=0) = 1$ and scales all other cases $g \neq 0$ accordingly.

The enhanced forward scattering for $f_I(\varphi_d)$ around $\varphi_d = 180^\circ$ is clearly visible for inclined disks. The polarization function $f_\phi^n(\varphi_d)$ has for backward scattering around $\varphi_d = 0^\circ$ and forward scattering around $\varphi_d = 180^\circ$ strongly reduced values in highly inclined disks when compared to the intensity as can be seen for the green and red curves in Fig. 6. At $\varphi_d = 90^\circ$ and 270° , the functions f_I and f_ϕ^n have (for given g) the same value for all inclinations because the scattering angles are always $\theta_{\varphi,i} = 90^\circ$ ($\cos \varphi_d = 0$ in Eq. 30).

The azimuthal dependence of the fractional polarization is given by

$$p_\phi^n(\varphi_d, i) = \frac{p_{\text{sca}}(\theta_{\varphi,i})}{p_{\max}} = \frac{f_\phi^n(\varphi_d, i, g)}{f_I(\varphi_d, i, g)}, \quad (33)$$

and this function does not depend on the asymmetry parameter g . This dependence is equivalent to Rayleigh scattering and is shown in Fig. 6 for completeness.

For the phase function f_Q and f_U one needs to consider that the Stokes Q_d and U_d parameters are defined in the disk coordinate system projected onto the sky while f_ϕ is given for the azimuthal angle φ_d for the x_d, y_d -coordinates of the disk mid-plane. For the splitting of $f_\phi(\varphi_d, i, g, p_{\max})$ into f_Q and f_U , the azimuthal angle ϕ_{xy} defined in the x - y sky plane must be used. The relation between φ_d and ϕ_{xy} is

$$\phi_{xy}(\varphi_d, i) = \arctan\left(\frac{\tan \varphi_d}{\cos i}\right). \quad (34)$$

The phase functions for Q_d and U_d are then equivalent to the conversion given in Eqs. 24 and 25:

$$f_Q(\varphi_d, i, g, p_{\max}) = -f_\phi(\varphi_d, i, g, p_{\max}) \cdot \cos(2\phi_{xy}(\varphi_d, i)) \quad (35)$$

$$f_U(\varphi_d, i, g, p_{\max}) = -f_\phi(\varphi_d, i, g, p_{\max}) \cdot \sin(2\phi_{xy}(\varphi_d, i)). \quad (36)$$

These azimuthal function of the ‘‘on-sky’’ Stokes parameters f_Q and f_U is shown in Fig. 7. The functions are characterized by their double wave, which for $i = 0^\circ$ are exact double-wave cosine $f_Q(\varphi_d) \propto -\cos 2\varphi_d$ and double-wave sine $f_U(\varphi_d) \propto -\sin 2\varphi_d$ functions. Deviations from the sine and cosine function become larger with increasing i , particularly for large asymmetry parameters g . The positive and negative sections of the $f_Q(\varphi_d)$ and $f_U(\varphi_d)$ functions correspond to the positive and negative polarimetric quadrants. The f_Q and f_U functions can also be expressed as normalized functions f_Q^n and f_U^n for $p_{\max} = 1$ and as fractional polarization p_Q^n and p_U^n equivalent to p_ϕ^n given above.

For the adopted HG_{pol} dust scattering phase function, these phase functions f_ϕ provide a universal description of the azimuthal flux and polarized flux dependence as a function of inclination i for all flat, optically thin, rotationally symmetric disks.

3.2.3. Disk-averaged scattering functions

The total intensity \bar{I} for our disk model can be conveniently calculated in r, φ_d -coordinates because the integration can be separated between the r -dependent scattering emissivity ϵ and the φ_d -dependent scattering phase function f_I according to

$$\bar{I} = 2\pi \int_0^\infty \epsilon(r) r dr \cdot \frac{1}{2\pi} \int_0^{2\pi} f_I(\varphi_d, i, g) d\varphi = \bar{\epsilon} \cdot \langle f_I(i, g) \rangle. \quad (37)$$

The first term represents the total scattering emissivity $\bar{\epsilon}$ of the disk, and the second term is the disk averaged scattering phase function for the intensity $\langle f_I(i, g) \rangle$.

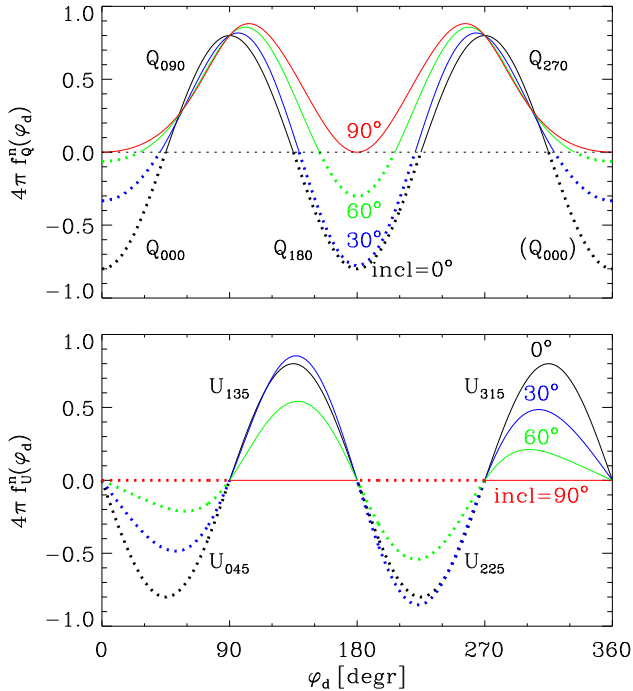


Fig. 7. Azimuthal dependence for the Stokes scattering phase functions $4\pi \cdot f_Q^n(\varphi_d, i, g)$ and $4\pi \cdot f_U^n(\varphi_d, i, g)$ for a rotationally symmetric, flat, optically thin disk with scattering asymmetry parameter $g = 0.3$ and inclinations $i = 0^\circ, 30^\circ, 60^\circ,$ and 90° .

For the integrated polarization parameters, the same type of relation can be used

$$\overline{Q}_\phi = \overline{\epsilon} \cdot \langle f_\phi(i, g, p_{\max}) \rangle, \quad (38)$$

$$\overline{Q}_d = \overline{\epsilon} \cdot \langle f_Q(i, g, p_{\max}) \rangle, \quad (39)$$

$$\overline{U}_d = \overline{\epsilon} \cdot \langle f_U(i, g, p_{\max}) \rangle. \quad (40)$$

The scale factor p_{\max} can be separated from the normalized versions of the disk-averaged scattering functions as

$$\langle f_\phi(i, g, p_{\max}) \rangle = p_{\max} \langle f_\phi^n(i, g) \rangle, \quad (41)$$

and similar for f_Q and f_U . The disk-averaged fractional polarization follows from

$$\langle p_\phi(i, g, p_{\max}) \rangle = p_{\max} \langle p_\phi^n(i, g) \rangle = \frac{\langle f_\phi(i, g, p_{\max}) \rangle}{\langle f_i(i, g) \rangle}, \quad (42)$$

and similar for p_Q or p_U , where the latter is always zero for rotationally symmetric disks. Unlike for the azimuthal dependence of the fractional polarization $p^n(\varphi_d, g)$, the disk-averaged parameters $\langle p_\phi^n(i, g) \rangle$ depend on the g -parameter because in this average g shifts the flux weight between disk regions producing higher or lower levels of scattering polarization.

3.3. Normalized quadrant polarization parameters

The Stokes Q_{xxx} and U_{xxx} quadrant polarization parameters correspond to the individual positive and negative sections of the $f_Q(\varphi_d)$ and $f_U(\varphi_d)$ disk phase function shown in Fig. 7. The relation between quadrant parameters and phase function follow the same scheme as for the disk-integrated quantities \overline{Q}_d and \overline{U}_d described by Eq. 37 but the integration is limited to the azimuthal

Table 2. Integration ranges for Stokes Q_d and U_d polarization quadrants for on-sky azimuthal angles $\phi_{xy} = \text{atan2}(y, x)$ and disk azimuthal angles $\varphi_d = \text{atan2}(y_d, x_d)$.

	$\int_{\phi_1}^{\phi_2} Q_d \text{ or } U_d(\phi_{xy}) d\phi$		$\int_{\varphi_1}^{\varphi_2} f_Q \text{ or } U(\varphi_d) d\varphi$	
	ϕ_1	ϕ_2	φ_1	φ_2
Q_{000}	-45°	45°	$-\text{atan}(\cos i)$	$\text{atan}(\cos i)$
Q_{090}	45°	135°	$\text{atan}(\cos i)$	$180^\circ - \text{atan}(\cos i)$
Q_{180}	135°	225°	$180^\circ - \text{atan}(\cos i)$	$180^\circ + \text{atan}(\cos i)$
Q_{270}	225°	315°	$180^\circ + \text{atan}(\cos i)$	$360^\circ - \text{atan}(\cos i)$
U_{045}	0°	90°	0°	90°
U_{135}	90°	180°	90°	180°
U_{225}	180°	270°	180°	270°
U_{315}	270°	360°	270°	360°

angle range φ_1 to φ_2 of a given quadrant instead of 0 to 2π . For Stokes Q_d , there is

$$Q_{xxx} = (\varphi_2 - \varphi_1) \int_0^\infty \epsilon(r) r dr \cdot \frac{p_{\max}}{\varphi_2 - \varphi_1} \int_{\varphi_1}^{\varphi_2} f_Q^n(\varphi_d, i, g) d\varphi. \quad (43)$$

The first term is the disk scattering emissivity ϵ integrated for the quadrant and the second term is the averaged f_Q^n scattering phase function for this quadrant. Because ϵ is independent of the azimuthal angle, the first term can be expressed as a fraction of the disk integrated emissivity $\overline{\epsilon} \cdot (\varphi_2 - \varphi_1)/2\pi$ and the equation takes the form

$$Q_{xxx} = \overline{\epsilon} p_{\max} \frac{1}{2\pi} \int_{\varphi_1}^{\varphi_2} f_Q^n(\varphi_d, i, g) d\varphi = \overline{\epsilon} p_{\max} Q_{xxx}^n(i, g), \quad (44)$$

where we introduce the normalized quadrant polarization Q_{xxx}^n . The same scaling factors $\overline{\epsilon}$ and p_{\max} are involved as for the equations for the integrated polarization parameters \overline{Q}_ϕ , \overline{Q}_d , and \overline{U}_d , and therefore Q_{xxx}^n and $\langle f_Q(i, g) \rangle$ are related with the same factors $\overline{\epsilon}$ and p_{\max} to observed quantities Q_{xxx} and \overline{Q}_d . The same formalism applies to the Stokes U_d quadrants.

According to Eq. 44, the normalized polarization quadrants $Q_{000}^n, Q_{090}^n, Q_{180}^n, Q_{270}^n$ and $U_{045}^n, U_{135}^n, U_{225}^n, U_{315}^n$ depend only on i and g as in the disk-averaged functions $\langle f_Q^n \rangle$ or $\langle f_U^n \rangle$. The azimuthal integration range φ_1 to φ_2 is of course different for each quadrant, as summarized in Table 2. For the Q_d -quadrants, the geometric projection effect introduces an inclination dependence for the integration boundaries φ_1 and φ_2 . For increased i , the fraction of the sampled disk surfaces $s_{xxx} = (\varphi_1(i) - \varphi_2(i))/2\pi$ in the left and right quadrants Q_{090}^n and Q_{270}^n is enhanced $s_{090} = s_{270} = 0.5 - \text{atan}(\cos i)/\pi$ and the disk surface fraction located in the front and back quadrants Q_{180}^n and Q_{000}^n is reduced $s_{000} = s_{180} = \text{atan}(\cos i)/\pi$, respectively (we note that $\text{atan}(\cos 0^\circ) = \pi/4$ and $\text{atan}(\cos 90^\circ) = 0$). There is no i -dependence for the splitting of the Stokes U_d quadrants, because the ‘‘left-side’’ back and front quadrants and the ‘‘right-side’’ back and front quadrants sample the same disk surface fraction $s_{045} = s_{135} = s_{225} = s_{315} = 0.25$ for all inclinations.

4. Calculation of disk polarization parameters

The previous section shows that the disk-integrated radiation parameters such as \overline{I} , \overline{Q}_ϕ and the quadrant polarization parameters Q_{xxx} and U_{xxx} can be expressed as disk-averaged phase functions $\langle f(i, g) \rangle$ and normalized polarization parameters $Q_{xxx}^n(i, g)$

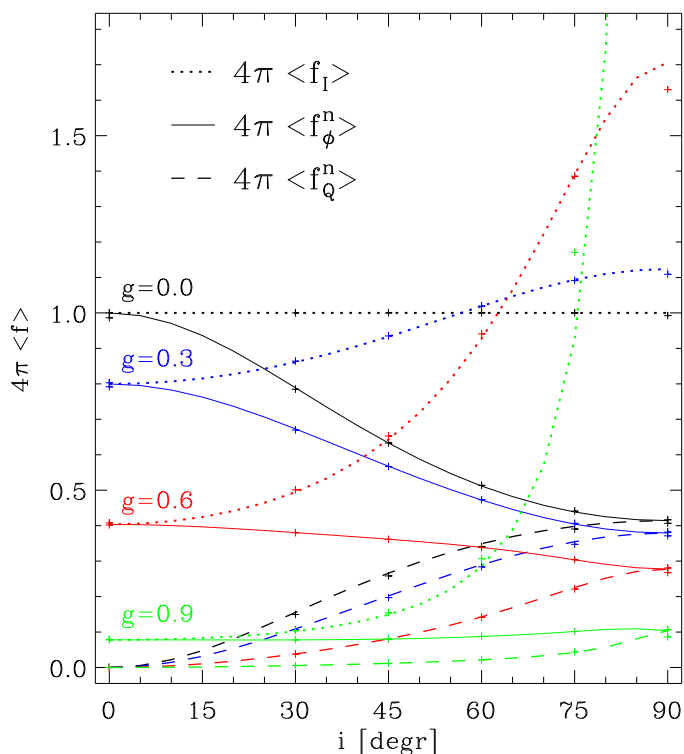


Fig. 8. Disk-averaged scattering phase functions for the intensity $4\pi\langle f_I \rangle$, the normalized ($p_{\max}=1$) azimuthal polarization $4\pi\langle f_\phi^n \rangle$, and the normalized Stokes Q_d flux $4\pi\langle f_Q^n \rangle$ versus the disk inclination for HG-asymmetry parameters $g = 0$ (black), 0.3 (blue), 0.6 (red), and 0.9 (green). Lines give the results for flat disks and crosses for vertically extended disk rings (Sect. 4.3, Fig. 11).

and $U_{xxx}^n(i, g)$ describing the azimuthal dependence of the scattering, and scale factors for the total disk-scattering emissivity $\bar{\epsilon}$ and the maximum scattering polarization p_{\max} .

This simplicity allows a concise but comprehensive graphical presentation covering the full parameter space of the disk model parameters for the intensity and polarization, including the newly introduced quadrant polarization parameters. The Appendix gives a few IDL code lines for calculation of the numerical values. In addition, we explore the deviation of the results from vertically extended disk models and from the flat disk models.

4.1. Calculations of the disk-averaged intensity and polarization scattering functions

The disk-averaged scattering phase functions $\langle f(i, g) \rangle$ are equivalent to the basic integrated quantities \bar{I} , \bar{Q}_ϕ , and \bar{Q}_d if normalized scale factors $\bar{\epsilon} = 1$ and $p_{\max} = 1$ are used (Eqs. 37 to 39). The functions $\langle f_I(i, g) \rangle$, $\langle f_\phi^n(i, g) \rangle$, and $\langle f_Q^n(i, g) \rangle$ are plotted in Fig. 8 as a function of inclination for the four asymmetry parameters $g = 0, 0.3, 0.6,$ and 0.9 . The plot includes the results from calculation of vertically extended, three-dimensional disk rings (crosses) for comparison, which are discussed in Sect. 4.3. The results for $\langle f(i, g) \rangle$ are multiplied by the factor 4π because this sets the special reference case for isotropically scattering dust $g = 0$ for all inclinations to $4\pi\langle f_I(i, 0) \rangle = 4\pi\langle f_\phi^n(i, 0) \rangle = 1$ and simplifies the discussion.

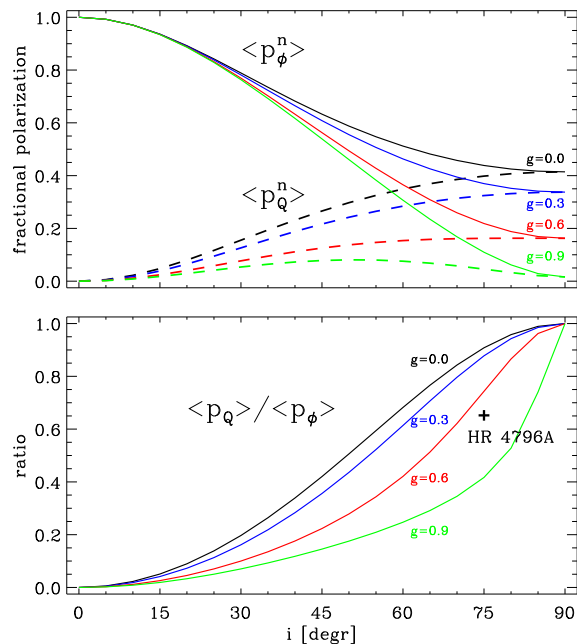


Fig. 9. Upper panel: Disk averages of the fractional azimuthal polarization $\langle p_\phi^n \rangle$ and the Stokes Q_d polarization $\langle p_Q^n \rangle$ normalized for $p_{\max} = 1$ for different asymmetry parameters and as function of inclination. Lower panel: Polarization ratios $\langle p_Q \rangle / \langle p_\phi \rangle = \bar{Q}_d / \bar{Q}_\phi$ and the corresponding measurement for HR 4796A.

For pole-on disks $i = 0^\circ$, there is $\langle f_\phi^n(0^\circ, g) \rangle = \langle f_I(0^\circ, g) \rangle$ for all g parameters because the scattering angle is $\theta = 90^\circ$ everywhere. For enhanced scattering asymmetry parameters $g > 0$ (but also for $g < 0$), the disk intensity is below the isotropic case $4\pi\langle f_I \rangle < 1$ for lesser and moderately inclined disks $i \lesssim 60^\circ$, because the enhanced forward scattering (or backward scattering) produces enhanced scattered flux in directions near to the disk plane and reduced flux for polar viewing angles.

The forward scattering enhances the scattered intensity to $4\pi\langle f_I \rangle > 1$ for $i \gtrsim 60^\circ$ and this effect becomes particularly strong for $g \rightarrow 1$ and $i \rightarrow 90^\circ$. This behavior is well known and produces a strong detection bias for high-inclination debris disks (e.g., Artymowicz et al. 1989; Kalas & Jewitt 1996; Esposito et al. 2020).

For the polarized flux $\langle f_\phi^n(i, g) \rangle$, an enhanced inclination does not produce an enhancement of the $\langle f_\phi \rangle$ signal because the strong increase in scattered flux from the forward scattering direction (or backward direction for $g < 1$) is predominantly unpolarized. For moderate asymmetry parameter $|g| \lesssim 0.6$, this causes an overall decrease of $\langle f_\phi \rangle$ with inclination (Fig. 8) while for extreme values $|g| \gtrsim 0.9$ the huge flux increase compensates for the lower fractional polarization for forward and backward scattering.

The phase function for the Stokes Q_d parameter $\langle f_Q^n(0^\circ, g) \rangle$ is zero for the pole-on view because of the symmetric cancellation of $+Q_d$ and $-Q_d$ signals. The function increases steadily with i (Fig. 8) and for $i = 90^\circ$ or edge-on disks there is $\langle f_Q^n(90^\circ, g) \rangle = \langle f_\phi^n(90^\circ, g) \rangle$, because all dust is aligned with the major axis and produces polarization in the $+Q_d$ direction.

Fractional polarization. The fractional polarizations $\langle p_\phi^n(i, g) \rangle$ and $\langle p_Q^n(i, g) \rangle$ in Fig. 9 can be deduced from the ratio of the phase functions shown in Fig. 8. Observationally, a fractional polariza-

tion determination requires a measurement of the integrated disk polarization and the integrated disk intensity.

As shown in Fig. 9, the fractional azimuthal polarization $\langle p_\phi^n(i, g) \rangle$ only depends to a very small extent on g for small inclinations $i \leq 35^\circ$ with deviations $< \pm 0.02$ and the i -dependence is well described by

$$\frac{\overline{Q}_\phi}{\overline{I}} = p_{\max} \langle p_\phi^n(i) \rangle \approx p_{\max} \cdot (\cos i)^{1.7}. \quad (45)$$

A measurement of the fractional azimuthal polarization for low-inclination disks is therefore equivalent to a determination of the p_{\max} -parameter.

The lower panel of Fig. 9 includes also the purely polarimetric ratio $\langle p_Q \rangle / \langle p_\phi \rangle = \overline{Q}_d / \overline{Q}_\phi$, which includes no scaling factor p_{\max} and systematic uncertainties from the polarimetric measurements might be particularly small. Therefore, the ratio $\overline{Q}_d / \overline{Q}_\phi$ can be used to determine the scattering asymmetry parameter g , if polarimetric cancellation effects for \overline{Q}_ϕ are taken into account for poorly resolved disks. For the extended disk HR 4796A, cancellation can be neglected, and we can use $\overline{Q}_d / \overline{Q}_\phi = 0.652 \pm 0.030$ ($\Sigma Q_{xxx} / \overline{Q}_\phi$ from Tab. 1) and the inclination $i = 75^\circ$, which yields a value of about $g = 0.7$ from Fig. 9. This method is useful for systems with $i \approx 30^\circ - 80^\circ$ because the separations between the g -parameter curves are quite large. The curves in Fig. 9 for flat disk models are not applicable for edge-on disks $i \gtrsim 80^\circ$ with a vertical extension (see Sect. 4.3).

4.2. Calculations of the normalized quadrant polarization parameters

The normalized quadrant polarization parameters Q_{000}^n , Q_{090}^n , Q_{180}^n , and U_{045}^n , U_{135}^n are plotted in Fig. 10 as a function of i for different g parameters. The “right-side” quadrants Q_{270}^n , U_{315}^n , U_{225}^n have the same absolute values as the corresponding “left-side” quadrants because of the disk symmetry. All values are multiplied by the factor 2π so that the reference case $g = 0$ and $i = 0^\circ$ is set to $2\pi |Q_{xxx}^n(0^\circ, 0)| = 2\pi |U_{xxx}^n(0^\circ, 0)| = 1$, similar to the normalization for the disk-averaged scattering function $4\pi \langle f_\phi^n(i, 0) \rangle$.

For pole-on disks, all the normalized quadrant polarization values have the same absolute value $|Q_{xxx}^n(0^\circ, g)| = |U_{xxx}^n(0^\circ, g)|$ for a given g . This value is lower for larger g -parameter because less light is scattered perpendicularly to the disk plane in the polar direction, as in the $\langle f_\phi^n \rangle$ function. For $i > 0^\circ$ the quadrant values show different types of dependencies on i and g .

As described in Sect. 3.3, for the Stokes Q_d quadrants the disk inclination introduces a geometric projection effect which increases the sampled disk area for the “left” and “right” quadrants for larger i , and therefore the Q_{090}^n and Q_{270}^n -values reach a maximum of $(Q_\phi^n/2)$ for $i = 90^\circ$. The areas for the front and back quadrants go to zero for $i \rightarrow 90^\circ$ and therefore so do the values Q_{180}^n and Q_{000}^n , but with a difference which depends strongly on g . The effect of the scattering asymmetry is already clearly visible for relatively small values, $g \approx 0.3$, and inclinations, $i \approx 10^\circ$, and becomes even stronger for larger g and i as can be seen from the enhanced $|Q_{180}|$ values relative to $|Q_{000}|$. A similar front-back quadrant effect also occurs for the U_d -components with enhanced absolute values for the front-side quadrant $|U_{135}|$ and reduced values for the backside quadrant $|U_{045}|$.

4.3. Comparison with three-dimensional disk ring models

The polarization parameters derived in the previous sections are calculated for geometrically flat disks because this simplifies the calculations enormously. Of course, real disks have a vertical extension but observations of highly inclined debris disks typically show a small ratio $h/r \lesssim 0.1$ (see e.g., Thébaud 2009). Therefore, the flat disk models could serve as an approximation for 3D disks, and we explore the differences. For this, we calculated models for a rotationally symmetric, optically thin disk ring with a central radius r_{ring} and a Gaussian density distribution for the ring cross-section,

$$\rho(r, h) = \rho_0 \exp(-[(r - r_{\text{ring}})^2 + h^2]/2\delta^2), \quad (46)$$

with full width at half maximum (FWHM) of $\Delta_{\text{FWHM}} = 2.355 \delta$. Figure 11 compares images of such 3D disk rings with $\Delta_{\text{FWHM}} = 0.2 r_{\text{ring}}$, $g = 0.6$, and different i with flat disk models. The vertical extension of the 3D model is most obvious for the edge-on ($i = 90^\circ$) case for which the flat disk model gives only a profile along the x -axis.

For $i < 90^\circ$, the differences between flat disks and vertically extended disks are already small for $i = 75^\circ$ and hardly recognizable for lower inclination. In particular, the values for the disk-averaged scattering functions $\langle f \rangle$ and the normalized quadrant polarization parameters Q_{xxx}^n and U_{xxx}^n are equal or very similar as can be seen in Figs. 8 and 10 where the results from the 3D disks are plotted as small crosses together with those from the flat disk models. The agreement is typically better than ± 0.01 . An example of a systematic difference between 3D disks and flat disks is a slightly lower value (about 0.01) for the azimuthal polarization $\langle f_\phi \rangle$ in Fig. 8 for pole-on ($i = 0^\circ$) 3D disks. For disks with a vertical extension, not all scatterings are occurring exactly in the disk midplane, but also slightly above and below where the scattering angle is smaller or larger than 90° and therefore $(1 - \cos^2 \theta)/(1 + \cos^2 \theta)$ in Eq. 20 is smaller than one. Another example is the reduced $\langle f_i \rangle$ for edge-on ($i = 90^\circ$) 3D disks, because less material lies exactly in front of the star where forward scattering would produce a strong maximum for large g -parameter. This is most visible for $g = 0.6$ (the effect is even stronger for $g = 0.9$ but this point is outside the plotted range). Similar but typically also very small effects are visible for the normalized quadrant polarization parameters in Fig. 10. The presence or absence of the vertical extension produces a strong difference for the Stokes U_d which is also clearly apparent in Fig. 11 for $i = 90^\circ$.

These comparisons show that the quadrant polarization parameters derived from flat, optically thin, rotationally symmetric disk models are for most cases essentially indistinguishable from those derived from 3D disk models with a vertical extension typical for debris disks. Only for edge-on or close to edge-on disks, $i \gtrsim 80^\circ$, can the vertical extension introduce significant differences, which needs to be taken into account.

5. Diagnostic diagrams for the scattering asymmetry g

The normalized quadrant polarization parameters and quadrant ratios for disk models using the HG_{pol} -function depend only on the scattering asymmetry parameter g and the disk inclination i as shown in Fig. 10. From imaging polarimetry of debris disks one can often accurately measure the disk inclination, and therefore the quadrant polarization parameters are ideal for the determination of g . The method described in this work for the single

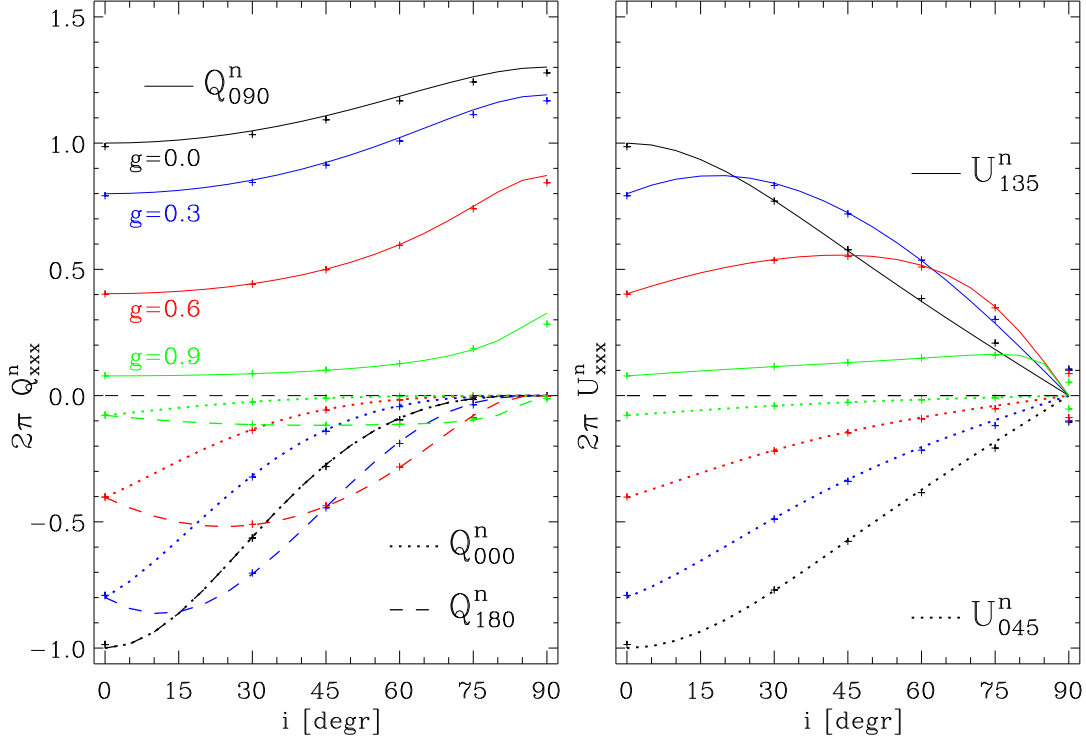


Fig. 10. Normalized ($p_{\max} = 1$, $\bar{\epsilon} = 1$) quadrant polarization parameters for $2\pi Q_{000}^n$, $2\pi Q_{090}^n$, $2\pi Q_{180}^n$ (left) and $2\pi U_{045}^n$, $2\pi U_{135}^n$ (right) as function of disk inclination and for the HG-asymmetry parameter $g = 0$ (black), 0.3 (blue), 0.6 (red), and 0.9 (green). Lines give the results for flat disks and crosses for vertically extended disk rings (Sect. 4.3, Fig. 11)

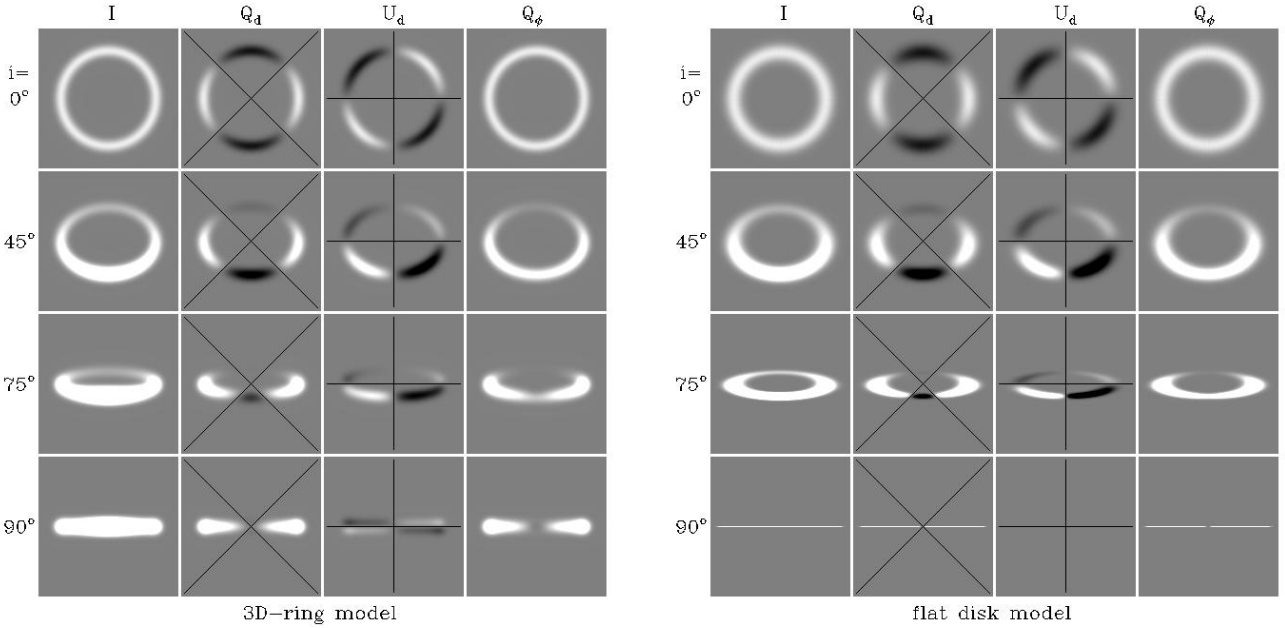


Fig. 11. Comparison of the 3D-ring model with the flat disk model. Left: I , Q_d , U_d and Q_ϕ for a 3D disk ring with a full width at half maximum density distribution of $\Delta_{\text{FWHM}}/r_{\text{ring}} = 0.2$. Scattering parameters are $g = 0.6$ and $p_{\max} = 1$ for inclinations $i = 0^\circ$, 45° , 75° and 90° . The same gray scale from $+a$ (white) to $-a$ (black) is used for all panels. The black lines in the Q_d and U_d panels indicate the polarization quadrants. Right: Same but for the flat disk model.

parameter HG_{pol} -function can be generalized to other, more sophisticated parameterizations for the polarized scattering phase function of the dust.

This diagnostic method is based on the strong assumption that the intrinsic disk geometry is rotationally symmetric, which

is often a relatively good assumption for debris disks, but there are also several cases known with significant deviations from axisymmetry (e.g., Debes et al. 2009; Maness et al. 2009; Hughes et al. 2018). This can affect the determination of the g -parameter and one should always assess possible asymmetries in the disk

symmetry using for example the left–right symmetry parameters Δ_{270}^{090} or Δ_{225}^{135} (Sect. 2.4).

5.1. Relative quadrant parameters

The azimuthal dependence of the scattering polarization can be described by the relative quadrant parameters Q_{xxx}/\bar{Q}_ϕ and U_{xxx}/\bar{Q}_ϕ . These parameters are directly linked to the normalized scattering phase functions f_Q^n , f_U^n , and f_ϕ^n for the polarization according to

$$\frac{Q_{xxx}}{\bar{Q}_\phi} = \frac{\bar{\epsilon} p_{\max} Q_{xxx}^n}{\bar{\epsilon} p_{\max} \langle f_\phi^n \rangle} = \frac{\frac{1}{2\pi} \int_{\phi_1}^{\phi_2} f_Q^n(\varphi_d, i, g) d\varphi}{\frac{1}{2\pi} \int_0^{2\pi} f_\phi^n(\varphi_d, i, g) d\varphi}, \quad (47)$$

and equivalent to U_{xxx}/\bar{Q}_ϕ .

The relative quadrant polarization parameters $|Q_{xxx}|/\bar{Q}_\phi$ and $|U_{xxx}|/\bar{Q}_\phi$ are plotted in Figure 12 as a function of g for disk inclinations $i = (0^\circ, 15^\circ, 30^\circ, 45^\circ, 60^\circ, \text{ and } 75^\circ)$. For pole-on disks, all relative quadrant values are equal to $(2\pi)^{-1}$ independent of the g -parameter, because of the normalization with \bar{Q}_ϕ .

With increasing g and i , the quadrant parameters show the expected steady increase for the front-side quadrants $|Q_{180}|/\bar{Q}_\phi$ and $|U_{135}|/\bar{Q}_\phi$ (red lines) and the steady decrease for the backside quadrants $|Q_{000}|/\bar{Q}_\phi$ and $|U_{045}|/\bar{Q}_\phi$ (blue lines). The separation between red and blue lines produces particularly large ratios for high inclination because the range of scattering angles extends from strong forward scattering to strong backward scattering.

For high inclination disks, the substantial contribution of forward and backward scattering strongly reduces the fractional scattering polarization in the front-side and back-side quadrants and the relative quadrant values are therefore $< (2\pi)^{-1}$ for small g . For the Q_{000} and Q_{180} quadrants, the reduction is further accentuated by the disk projection which reduces the sampled disk area for inclined disks. Strong forward scattering $g \rightarrow 1$ compensates these two effects to a certain degree for the front-side quadrants (red curves), while it further diminishes the flux in the (blue) back side quadrants.

The two positive Q_d quadrant parameters Q_{090}/\bar{Q}_ϕ and Q_{270}/\bar{Q}_ϕ depend mainly on the disk inclination. For higher inclination, a greater area of the disk is included in these two quadrants and therefore their relative contribution to the total polarized flux Q_{090}/Q_ϕ increases from $(2\pi)^{-1}$ for $i = 0^\circ$ to 0.5 for $i = 90^\circ$. For edge-on systems, there is $2 \cdot Q_{090} = \bar{Q}_\phi = \bar{Q}_d$ or all polarized flux of a disk is located only in the left and right quadrants Q_{090} and Q_{270} .

Figure 12 includes the relative quadrant parameters measured for HR 4796A from Table 1. This disk has an inclination of about 76° (e.g., Chen et al. 2020; Milli et al. 2019) and the $i = 75^\circ$ -lines match this value well. For Stokes Q_d the front side value $|Q_{180}|/\bar{Q}_\phi$ is very sensitive for the determination of the g -parameter because the corresponding curve in Fig. 12 is steep. This results in a value of $g = 0.72 \pm 0.03$ with a relative uncertainty of only about $\pm 4\%$, despite the relatively large measuring error of about $\pm 13\%$ for $|Q_{180}|/\bar{Q}_\phi$. The polarization signal is strong near the major axis and the corresponding quadrant values $|Q_{090}|/\bar{Q}_\phi$ and $|Q_{270}|/\bar{Q}_\phi$ can be measured with high precision of roughly $\pm 3\%$. However, because the $|Q_{090}|/\bar{Q}_\phi$ curve is rather flat in Fig. 12, the resulting uncertainty on the derived g -values is also about $\pm 3\%$. The obtained g -values for $|Q_{090}|/\bar{Q}_\phi = 0.62$ and

$|Q_{270}|/\bar{Q}_\phi = 0.72$ differ significantly because of the described deviation of the HR 4796A disk geometry from axisymmetry.

For the backside quadrant, only an upper limit of about $|Q_{000}|/\bar{Q}_\phi < 0.04$ could be measured. This limit is not useful for constraining the g -value because expected values for an inclination of 75° are very low, namely $|Q_{000}|/\bar{Q}_\phi \approx 0.004$ for $g = 0.0$ and ≈ 0.001 for $g = 0.6$, and the corresponding curve is below the plot range covered in Figure 12.

The relative quadrant values of HR 4796A for Stokes U_d yield low asymmetry parameters $g \approx 0.4$ for the back-side quadrants $|U_{045}|/\bar{Q}_\phi$ and $|U_{315}|/\bar{Q}_\phi$, and larger values of $g \approx 0.5$ and $g \approx 0.7$ for the front side, with again a significant left–right asymmetry.

5.2. Quadrant ratios

The scattering asymmetry g can also be derived from quadrant ratios describing the brightness contrast between the front and back sides of the disk as shown in Fig. 13, which includes the measurements from HR 4796A.

High-quality determinations of g are achieved if the front- and the back-side quadrant polarizations can be accurately measured. For low-inclination systems, this should be possible for ratios like $|Q_{000}|/|Q_{180}|$ or $|U_{045}|/|U_{135}|$ where both the front side and back side are bright. For high-inclination systems, as in HR 4796A, the back side can be faint and the ratios $|Q_{000}|/|Q_{180}|$ or $|U_{045}|/|U_{135}|$ are small ($\lesssim 0.1$) and therefore difficult to measure accurately. As an alternative, one can use ratios based on the bright quadrants like $|Q_{090}|/|Q_{180}|$ or $|Q_{090}|/|U_{135}|$ or equivalent ratios using the right-side quadrants Q_{270} and U_{225} . Many aspects of the diagnostic diagrams plotted in Fig. 13 are similar to the description of the relative quadrant parameters in the previous section.

5.3. Polarized scattering phase function for HR 4796A

5.3.1. Comparison of different g determinations

The measured quadrant polarization parameters for HR 4796A can be used to strongly constrain the asymmetry parameter g of the adopted HG_{pol} scattering phase function $f_\phi(\theta)$, but only for the θ -range sampled by the used quadrant parameters (see also Hughes et al. 2018). The flux-weighted distribution of scattering angles θ sampled by a quadrant strongly depends on inclination i , but also on g as illustrated in Fig. 14. Indeed, all quadrants of a nearly pole-on disks probe $f_\phi(\theta)$ only near the scattering angle of 90° , while some quadrants probe a large θ -range for strongly inclined disks.

We define the median angle θ_{med} for the angle that represents the 50th percentile of a cumulative polarized intensity distribution covered by one quadrant. The back and front quadrants Q_{000} and Q_{180} sample a narrow range, the median angle θ_{med} is close to the most extreme backward and forward scattering angle $\theta_{\text{med}} \approx 90^\circ \pm i$ for a disk with inclination i , and θ_{med} are essentially identical for different g . The ranges of scattering angles θ covered by the quadrants Q_{090} , U_{045} , and U_{135} are very broad for larger i and the θ_{med} depend significantly on g as shown in Fig. 14. For example, $\theta_{\text{med}}(Q_{000})$ is 90° for isotropic scattering, and becomes smaller for $i \rightarrow 90^\circ$ and $g \rightarrow 1$ as indicated by the colored θ_{med} points (diamonds) and the dotted lines.

The quadrants U_{045} and U_{135} sample the back- and front-side parts of the disk and their θ_{med} -angles lie between those of the Q_d -quadrants. The front-side quadrant also shows a strong

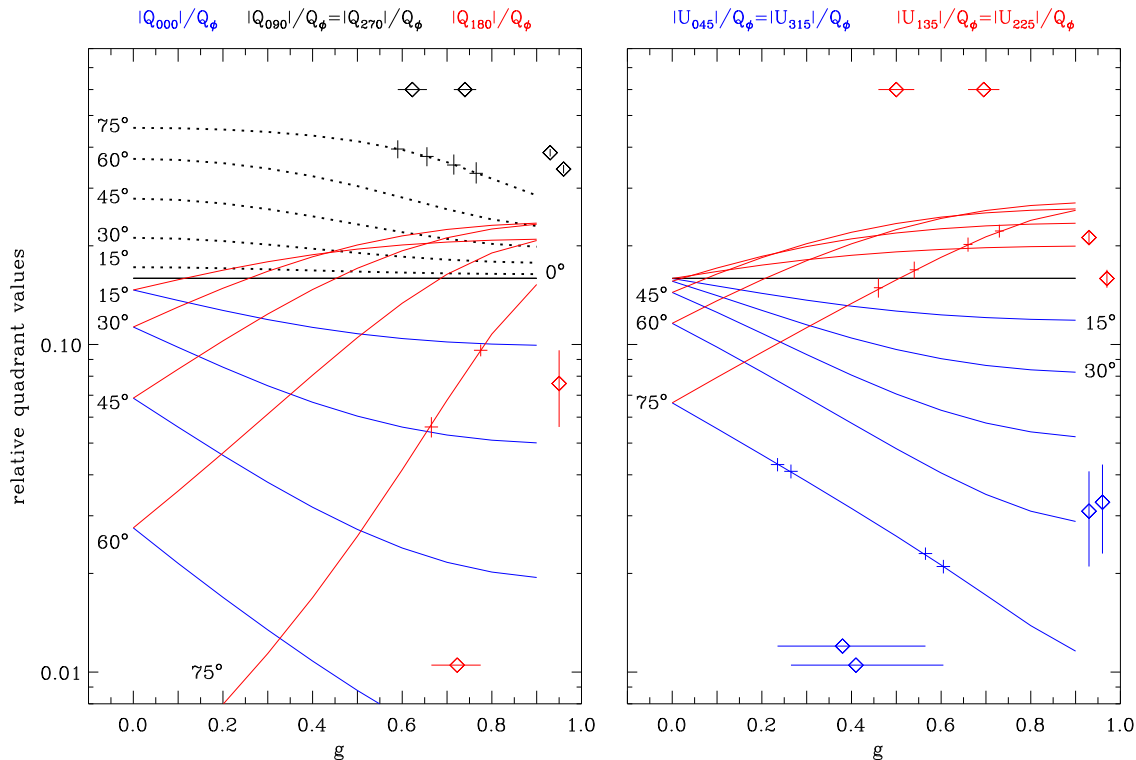


Fig. 12. Relative quadrant polarization values $|Q_{000}|/\bar{Q}_\phi$ (blue), $|Q_{090}|/\bar{Q}_\phi$ (black) $|Q_{180}|/\bar{Q}_\phi$ (red) on the left and $|U_{045}|/\bar{Q}_\phi$ (blue), $|U_{135}|/\bar{Q}_\phi$ (red) on the right for flat disk models with different i and as a function of the scattering asymmetry parameter g . The measured values for HR 4796A are given on the right side in each panel and the corresponding g -parameter is given at the top or bottom using the $i = 75^\circ$ curves for these derivations.

tendency towards smaller $\theta_{\text{med}}(U_{135})$ values for larger g and i , as in the Q_{090} -quadrant, while the g -dependence of $\theta_{\text{med}}(U_{045})$ is much smaller.

Figure 15 shows the g -parameters obtained for HR 4796A as a function of the θ -angle probed by the used quadrant parameters. The angle θ corresponds for relative quadrant parameters to θ_{med} for $i = 75^\circ$ and $g = 0.6$ as given in Fig. 14 and the horizontal uncertainty bar spans two-thirds of the plotted θ -distribution (from the 16.6 to the 83.3 percentiles). For the quadrant ratios, the adopted θ -values are the mean of the θ_{med} of the two quadrants and the horizontal bars illustrate their separation. In principle, one should consider for the θ_{med} -values the systematic trend of $g(\theta_{\text{med}})$ from higher g -values (≈ 0.7) for forward-scattering quadrants to lower values (≈ 0.4) for the backward scattering quadrants. We neglect this effect which would introduce θ_{med} shifts of about -5° for U_{135} and U_{225} , shifts of about $+5^\circ$ for Q_{090} and Q_{270} , and smaller shifts for the other quadrants.

Figure 15 shows for HR 4796A a systematic dependence of the derived g -parameters with scattering angle θ . The results from the relative quadrant parameters and the quadrant ratios are roughly consistent. The colors indicate measurements for the left (blue) and right (red) sides of the disk and g -values differ significantly between the two sides for $\theta_{\text{med}} = 35^\circ$ and 70° because of the left–right disk brightness asymmetry. On the fainter side, this effect reduces the derived g -value for U_{225}/\bar{Q}_ϕ , while g is enhanced for Q_{270}/\bar{Q}_ϕ because the intrinsic faintness of Q_{270} mimics a disk with relatively little 90° -scattering because of the normalization with \bar{Q}_ϕ . The intrinsic left–right brightness asymmetry of HR 4796A has less impact on the g determination based on quadrants ratios from the same side. This redundancy helps

to disentangle the effects of the scattering asymmetry g from geometric or left–right disk brightness asymmetries.

5.3.2. A “mean” asymmetry parameter g for HR 4796A

The clear trend of the derived g -parameter with scattering angle θ for HR 4796A in Fig. 15 reveals that the used HG_{pol} -function is an oversimplified description of the polarized scattering phase function for this object. For fainter or less well resolved disks, and for those with low inclination, it may not be possible to recognize such systematic deviations from a HG_{pol} function, and for all these cases the derived g -value from the HG_{pol} -function could serve as a good starting point for the analysis of quadrant polarization parameters.

Therefore, for HR 4796A we also derive a “mean” value for the HG asymmetry parameter g despite the discussed trend. To this end, for the seven measured relative quadrant values $|U_{045}|/\bar{Q}_\phi$, $|Q_{090}|/\bar{Q}_\phi$, $|U_{135}|/\bar{Q}_\phi$, $|U_{180}|/\bar{Q}_\phi$, $|U_{225}|/\bar{Q}_\phi$, $|U_{270}|/\bar{Q}_\phi$, and $|U_{315}|/\bar{Q}_\phi$ from Table 1, we determine the best-fitting g -asymmetry parameter for the adopted disk inclination $i = 75^\circ$. This yields $\text{HG}_{\text{pol}}(i = 75^\circ, g = 0.65)$ with a weighted sum of squared deviations of $\chi^2 = 15.4$, and the corresponding calculated and measured values are plotted in Fig. 16a. The differences between the models are more visible in Fig. 16b, where the deviations of data points and calculations from the best-fit model are shown. The large χ^2 -value indicates that the adopted HG_{pol} -fit does not describe the data well because of the significant left–right asymmetry between $|Q_{090}|$ and $|Q_{270}|$, or $|U_{135}|$ and $|U_{225}|$ at the level of about 4σ (σ : standard deviations), which cannot be described with an axisymmetric disk model.

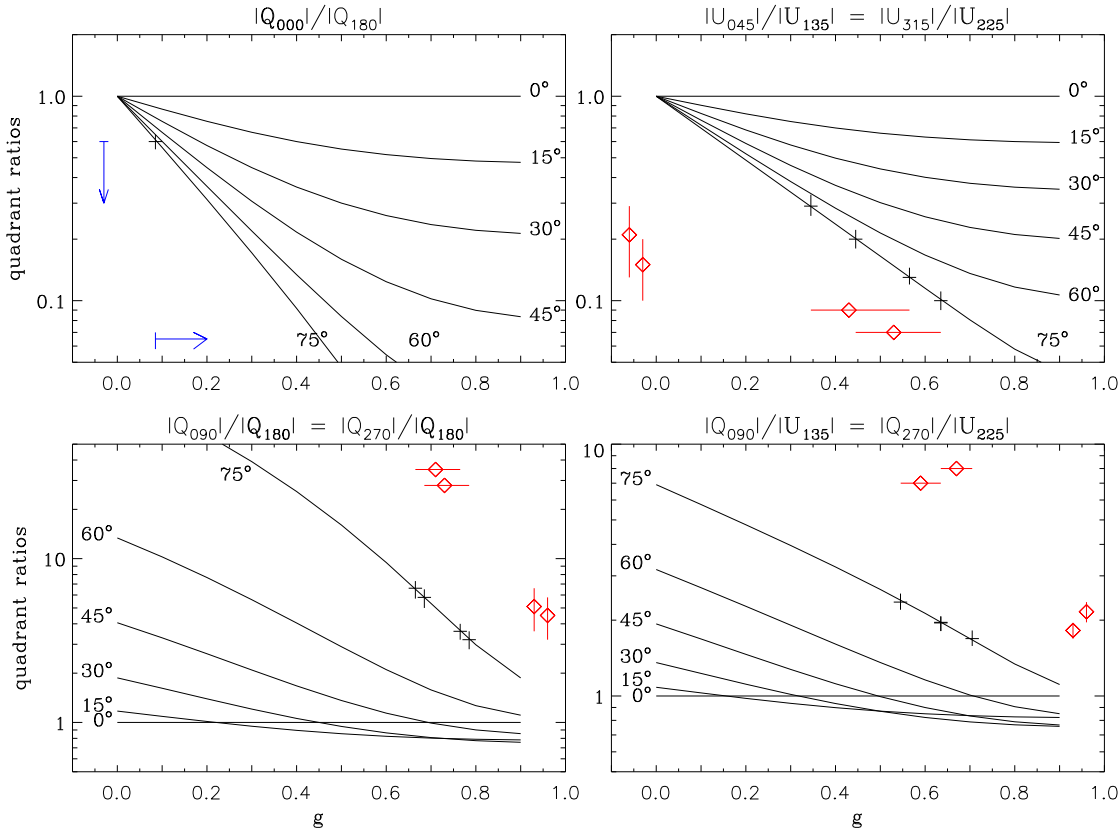


Fig. 13. Quadrant polarization ratios for flat disk models for $|Q_{000}|/|Q_{180}|$, $|U_{045}|/|U_{135}|$, $|Q_{090}|/|Q_{180}|$, and $|Q_{090}|/|Q_{135}|$ with measured values from HR 4796A (similar to Fig. 12).

Additionally, the best fit underestimates the quadrant values at small ($\theta_{\text{med}} = 16^\circ$) and large (124°) scattering angles. Panel (b) also includes the best-fit results for slightly different disk inclinations $\text{HG}_{\text{pol}}(i = 73^\circ, g = 0.60)$ and $\text{HG}_{\text{pol}}(i = 77^\circ, g = 0.71)$, which differ very little and produce deviations between fit and data that are similar to the $i = 75^\circ$ solution. The corresponding Henyey-Greenstein scattering phase functions HG_{pol} (or $f_\phi(\theta)$) are given in panel (c), while panel (d) shows the HG intensity function ($f_I(\theta)$) for the best quadrant solution for $i = 75^\circ$ and the solution from Milli et al. (2019).

Fortunately, we can compare the result from the quadrant parameter fitting with the analysis of the same HR 4796A data by Milli et al. (2019). They extracted from the polarimetric imaging data a detailed phase curve shown in Fig. 16c covering the scattering angle range $\theta = 13^\circ$ to 145° . They also fitted the extracted phase curve with a single parameter HG_{pol} -function and obtained an asymmetry parameter of $g = 0.43$ which is much smaller than our value of $g = 0.65$ (Fig. 16c). An important reason for this discrepancy is the sampling of the scattering angles of the data used for the fitting. In this work, the fitting is based on seven quadrant polarization values—for a disk with $i = 75^\circ$ and $g > 0.4$ —which are strongly biased towards small θ -values because of the forward “distorted” distribution of the polarized flux. In addition, the back-side quadrants U_{045} and U_{315} are weak and the corresponding measurements have a low signal-to-noise ratio of $S/N < 5$ and therefore a small weight. Thus, the fit to the quadrant values predominantly samples the range $\theta \approx 16^\circ$ to 67° of the scattering phase function. The analysis of Milli et al. (2019) samples a much broader range and particularly also more backward scattering angles. Therefore, the

result of these latter authors of $g = 0.43$ closely matches the g -values derived in this work by the quadrant ratios $|U_{045}|/|U_{135}|$ and $|U_{315}|/|U_{225}|$ (Fig. 13). On the other hand, the HG_{pol} -fit of Milli et al. (2019) underestimates their extracted phase function in the forward-scattering range $\theta \approx 16^\circ$ to 35° . This comparison illustrates the bias effect that can be introduced by different kinds of phase curve sampling, if the adopted model curves $f_\phi(\theta)$ do not match well the real scattering phase function of the dust.

5.3.3. A fit with a double HG_{pol} -function

A better agreement between measured and calculated quadrant values can be obtained using a double HG-function for the dust scattering

$$f_I(\theta, g_1, g_2, w) = w f(\theta, g_1) + (1 - w) f(\theta, g_2), \quad (48)$$

because three parameters provide more freedom for the polarized phase curve $f_\phi^n(g_1, g_2, w) = f_I(\theta, g_1, g_2, w) \cdot p_{\text{sca}}(\theta)$ in the quadrant fitting. Calculating quadrant polarization values for $i = 75^\circ$ and a grid of phase function parameter g_1 and $w \in [0.00, 0.01, \dots, 1.00]$, and $g_2 \in [-1.00, -0.99, \dots, g_1]$ gives a best-fit solution of $(g_1, g_2, w) = (0.78, -0.09, 0.85)$ with $\chi^2 = 10.2$ which is plotted in Fig. 17.

Compared to the case of the best single parameter HG_{pol} function (Fig. 16), this fit does not underestimate the relative quadrant values at $\theta_{\text{med}} = 16^\circ$ and 124° and passes in the middle of the discrepant quadrant values at 35° and 67° for the left and right disk sides (see Fig. 17a and b). The corresponding polarized scattering phase function $f_\phi(\theta)$ in Fig. 17c has a much

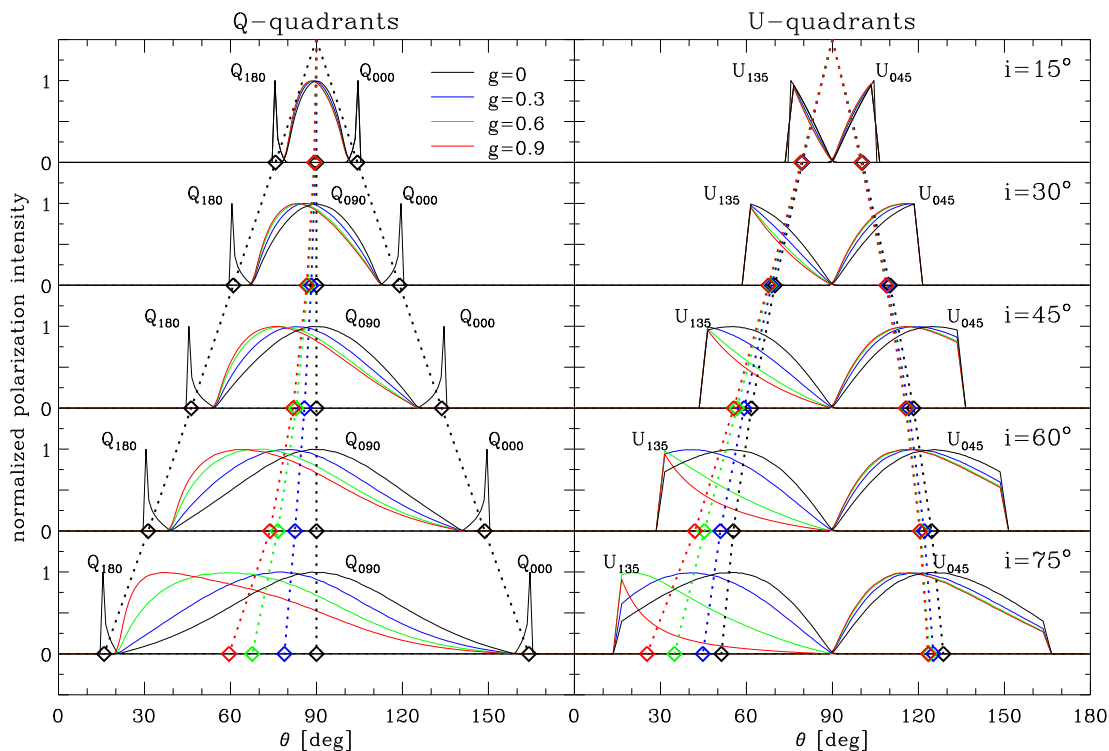


Fig. 14. Angular distribution of the polarized intensity in the polarization quadrants for $i = 15^\circ, 30^\circ, 45^\circ, 60^\circ$ and 75° and different asymmetry parameter g (colors). For quadrants Q_{000} and Q_{180} only the case $g = 0$ is shown, because differences for other g -parameters are very small. The distributions are normalized for each quadrant individually. For the quadrants Q_{000} , U_{045} , and U_{135} , the median angles θ_{med} (diamonds) for large g -values increase with inclination as illustrated with the dotted lines.

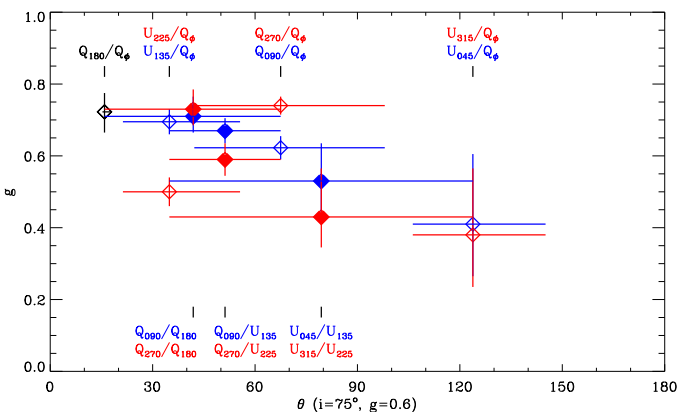


Fig. 15. Scattering asymmetry parameters for HR 4796A derived from relative quadrant parameters (open symbols) and quadrant ratios (filled symbols) as a function of the θ_{med} or the mean of θ_{med} , respectively. Colors indicate measurements from the left or SW (blue) and the right or NE (red) disk sides.

wider peak extending from $\theta \approx 20^\circ$ to $\approx 90^\circ$, closely matching the directly extracted phase curve from Milli et al. (2019).

It is interesting to compare our results with the double HG_{pol} function obtained by Milli et al. (2019) from the fit to the detailed phase-curve extraction which is included in Fig. 17 as a green dashed line. Unfortunately, there is an error in the indicated fit parameters in Fig. 5 of Milli et al. (2019) but the plotted fit curve is correct. The fit parameters should be $(g_1, g_2, w)_{\text{Milli}} =$

$(0.83, 0.09, 0.81)$ (J. Milli, personal communication) which also provide a very good fit to the quadrant polarization values derived in this work as shown in Fig. 17(a) and (b).

The good agreement between the double HG_{pol} -fits of Milli et al. (2019) and the solution found for the quadrant polarization values shows that the selection of a more appropriate scattering phase function strongly reduces the large difference in the deduced g -determination described in Sect. 5.3.2 using only the single HG_{pol} function. It should also be noted that the polarized phase function fit $f_\phi(\theta)$ of Milli et al. (2019) does not consider the left–right asymmetry of the disk in HR 4796A and therefore the phase curve uncertainty attained by these latter authors is larger than their measurement uncertainties. It seems likely that the azimuthal polarization signal extracted by Milli et al. (2019) would probably allow the determination of a better constrained empirical $f_\phi(\theta)$ -function for HR 4796A if the significant azimuthal dependence on the dust density is included in the fitting. Using a more detailed disk model for the fitting of the derived quadrant polarization parameters seems to be less useful because of the small number of measured values, a matter that is discussed further in Sect. 6.3.

This example shows that selecting a good model fit function is important for the analysis of the quadrant polarization parameters and this should be investigated in more detail. The double HG_{pol} is probably not an ideal choice, because in the intensity scattering function significant weight is given to the forward and backward scattering angles, which produce less polarization and therefore contribute less to the signal in the corresponding polarization quadrants Q_{000} or Q_{180} . This could explain the substantial

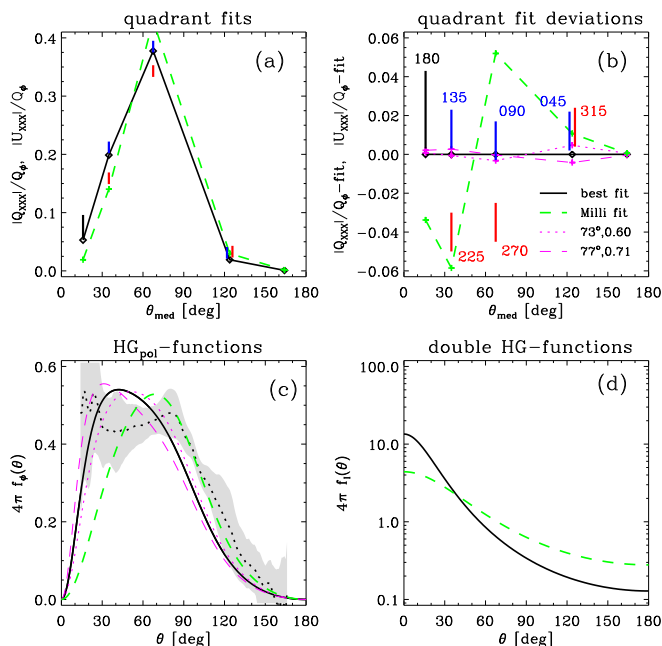


Fig. 16. (a) Comparison of the best single parameter HG_{pol} fit model for fixed $i = 75^\circ$ and measured relative quadrant polarization parameters for HR 4796A. (b) Deviations from the best-fitting $\text{HG}_{\text{pol}}(i = 75^\circ, g = 0.65)$ for the measured values, for the best fits for slightly different disk inclinations $\text{HG}_{\text{pol}}(i = 73^\circ, g = 0.60)$ and $\text{HG}_{\text{pol}}(i = 77^\circ, g = 0.71)$ and for the HG_{pol} fit from Milli et al. (2019) (green dashed line). (c) HG_{pol} phase functions and the directly extracted phase function $f_\phi(\theta)$ (dotted black line) with corresponding uncertainty range (grey shaded area) from Milli et al. (2019). (d) HG intensity phase functions. The measured quadrant values and the different fit curves are identified in panel (b).

differences for $\theta < 16^\circ$ or for $\theta > 124^\circ$ between the two derived best-fitting functions in Fig. 17d where the quadrant parameters provide no or only weak constraints on the shape of the scattering phase function.

In a future study, alternative polarized scattering phase functions $f_\phi(\theta)$ should be investigated for the fitting of polarimetric data, which give more weight to intermediate scattering angles $\theta \approx 90^\circ \pm i$. Such a curve should also consider deviations of the fractional scattering polarization from a symmetric curve (Rayleigh-like) with respect to $\theta = 90^\circ$ as already derived from observations of HR 4796A by Perrin et al. (2015) and Arriaga et al. (2020). Considering this could be particularly important when constraining $f_\phi(\theta)$ for the dust in debris disks with smaller inclinations and a more limited observable range of θ -angles.

6. Discussion

6.1. New polarization parameters for circumstellar disks

In recent years, the scattering light of many proto-planetary and debris disks has been spatially resolved with high-resolution polarimetric imaging using modern AO systems at large telescopes (Schmid 2021). Unfortunately, the presented results for the measurements of the polarized light from circumstellar disks are highly heterogeneous and are rarely flux calibrated, and it is therefore very difficult to compare the results from different studies for a systematic investigation of disks.

The main motivation of the present paper is the promotion of a photo-polarimetric parameter system which should help to ho-

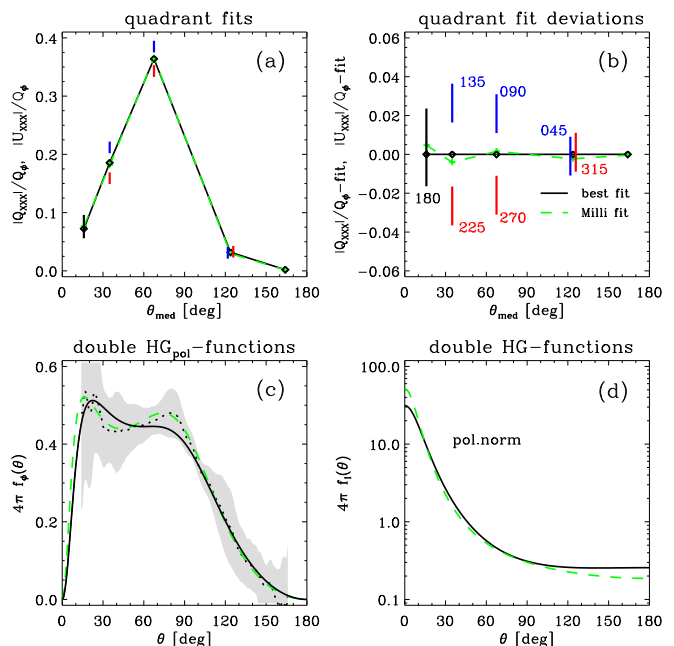


Fig. 17. Same as Fig. 16 but for the best-fitting double HG_{pol} scattering phase function $(g_1, g_2, w)_A = (0.78, -0.09, 0.85)$ for $i = 75^\circ$ and the function obtained by Milli et al. (2019) (dashed green lines): (a) calculated and measured relative quadrant values; (b) deviations of obtained values from the best-fitting solution; (c) double HG_{pol} phase function for the fits and the directly extracted curve from Milli et al. (2019) (dotted line and grey uncertainty range); (d) corresponding intensity phase functions.

mogenize the polarimetric measurements for circumstellar disks and allow more straightforward comparisons between measurements of different disks and model results. The introduced quadrant polarization parameters $Q_{000}, Q_{090}, Q_{180}, Q_{270}$ and $U_{045}, U_{135}, U_{225}, U_{315}$ are defined for the Stokes Q_d and U_d parameters aligned with the apparent major and minor axis of the projected disk; they are based on the “natural” quadrant pattern produced by circumstellar scattering and measure within these quadrants the integrated Stokes Q_d and Stokes U_d flux, respectively.

These eight quadrants are very well suited for the description of the azimuthal dependence of the polarization signal of disks, except for edge-on or nearly edge-on systems. Furthermore, they can be used to quantify geometric deviations of the disk from axisymmetry from differences between left and right quadrants or characterize the disk inclination effects and the dust scattering asymmetry from ratios between back-side and front-side quadrants.

This disk characterization only requires differential polarization measurements, like relative quadrant parameters Q_{xxx}/\bar{Q}_ϕ and U_{xxx}/\bar{Q}_ϕ , or quadrant ratios like Q_{000}/Q_{180} . No absolute flux calibration with respect to the intensity of the star I_{star} or the disk \bar{I} are required and therefore one can also use polarimetric imaging of disks obtained in coronagraphic mode or with the central star saturated. In addition, the eight quadrant parameters are partially redundant and offer multiple options for the characterization of a disk, meaning that problems with a particular quadrant, for example because of the peculiarities of a disk or observational effects, can be mitigated.

The quadrant polarization measurements should be particularly well adapted for well-resolved, extended, low-surface-brightness debris disks, which are relatively common (Espos-

ito et al. 2020). The integration of the Q and U polarization for entire quadrants helps to improve the signal, and restricting the measurements of the azimuthal dependence to a few values is appropriate for a faint source where it is hard to get sufficient signal for a detailed characterization. Of course, the calibration of the polarization zero point must be determined very accurately for faint sources and this can be achieved for many debris disks because the central star is often a very good zero polarization reference source.

Model calculations exploring the parameter space for the dust scattering in circumstellar disks are of particular importance for advancing our understanding of the properties of the scattering dust in disks. The quadrant polarization parameters are very well suited to characterizing the azimuthal dependence of the polarization signal for different models. Because these model results can be expressed as relative values or ratios, they can be readily compared with each other for the evaluation of dependencies on the scattering asymmetry for optically thin disks or the angle dependencies of the surface reflectivity in optically thick disks, even if parameters such as stellar illumination, disk size, or radial dust density distribution in optically thin disks are different.

The modeled values can also be compared with observations, but important issues are the PSF smearing and polarimetric cancellation effects between positive and negative quadrants. This can significantly reduce the measurable polarization for poorly resolved disks (Schmid et al. 2006; Tschudi & Schmid 2021) and change the appearance of the Q and U quadrant patterns of inclined or asymmetric disks (Heikamp & Keller 2019). For example, for the Stokes Q_d quadrants, the PSF convolution reduces the total signal of the positive quadrants Q_{090} and Q_{270} by the same amount as it enhances the signal (less negative signal) in the negative quadrants Q_{000} and Q_{180} ; the same is true for the Stokes U_d quadrants. If the PSF is well known for a given observation then the smearing and cancellation effects can be taken into account accurately in order to minimize the introduced effects (Tschudi & Schmid 2021).

The measurements of the quadrant polarization parameters for circumstellar disks provide a simple and model-independent method for the description of the azimuthal distribution of the scattering polarization and the obtained results can be easily tested by comparing the measured and calculated model values. Similarly, the quality of the measured quadrant data can be verified with alternative measurements of the same target. Of course, a detailed analysis of the polarimetric imaging data with 2D synthetic model images would provide a more detailed comparison, but this is a very laborious procedure which requires detailed knowledge of the observational effects for each data set and a good understanding of the modeling aspects for each individual disk (see e.g., Milli et al. 2019; Olofsson et al. 2020; Chen et al. 2020, for the case of HR 4796A). Therefore, it appears attractive to base a quick analysis of many disks on the simple quadrant polarization parameters. Once measured and corrected for the PSF smearing, they remain unchanged until higher quality measurements become available and the interpretation of the measurements obtained can be continuously improved if additional information about the corresponding disk model can be taken into account.

6.2. Investigation of debris disks

The usefulness of the quadrant polarization parameters is tested in this work with simple models of debris disks and with observations of the prototype debris-disk system HR 4796A. De-

bris disks are optically thin and therefore the azimuthal dependence of the polarization signal depends directly on the polarized scattering phase function $f_\phi(\theta)$ of the dust. Because the quadrant polarization parameters measure the azimuthal dependence, they are ideal for determining $f_\phi(\theta)$. This is shown with model calculation of flat axisymmetric debris disks using the simple HG_{pol} function for the parameterization of the polarized scattering phase function $f_\phi(\theta, g)$. For optically thin, rotationally symmetric disks, the azimuthal dependence of the polarization signal can be directly described by a disk scattering phase function $f_\phi(\varphi_d, i, g)$, which only depends on the disk inclination i and the scattering asymmetry parameter g of the HG function. This function also defines the relative quadrant polarization values $Q_{xxx}(i, g)/\bar{Q}_\phi(i)$ as an eight-parameter condensation of the azimuthal polarization dependence, from which one can also derive quadrant ratios like $Q_{000}(i, g)/Q_{180}(i, g)$ as alternative results. These parameters yield a measure for the dust-scattering asymmetry for a given i and corresponding diagnostic diagrams have been calculated for relative quadrant values and quadrant ratios. If the selected HG_{pol} function is an appropriate parametrization for the dust scattering of an observed debris disk then all the measured quadrant parameters should yield the same g parameter. The same method can be applied for investigations of other scattering phase functions.

We tested the polarized phase-curve determination based on the quadrant polarization parameters for data of the “prototype” debris disk around HR 4796A from Milli et al. (2019). First, we noticed a significant disk asymmetry between the “left” and “right” sides with respect to the minor axis of the disk ring as projected on the sky. We did not consider this disk asymmetry and simply derived a “mean” scattering phase curve accepting that this introduces some uncertainties in the phase curve analysis. The diagnostic diagrams for the HG_{pol} scattering phase function were used and the obtained g parameter determination shows a clear trend from high values $g \approx 0.7$ for quadrants sampling small scattering angles $\theta \approx 30^\circ$ to lower values $g \approx 0.4$ for larger scattering angles $\theta \approx 120^\circ$. This is a clear indication that the adopted HG_{pol} -scattering function is not adequately describing the dust in HR 4796A. The over-simplified fit model introduces strong bias effects responsible for significant differences between the g -value determination based on a detailed phase-curve extraction and the one based on the quadrant parameters.

As alternative, we used a three-parameter double HG_{pol} function as description for the dust scattering $f_\phi(\theta)$. The best fit solution to the quadrant values that we find is in good agreement with the detailed phase curve extraction of Milli et al. (2019) based on the same data. This is surprising because the covered θ -range for the phase curve from about 16° to 164° is large for the high-inclination ($i \approx 75^\circ$) system HR 4796A and a characterization of $f_\phi(\theta)$ based on a few quadrant values yields only a relatively coarse θ resolution. The main reason the detailed $f_\phi(\theta)$ -extraction of Milli et al. (2019) is not clearly superior when compared to the quadrant method is the significant deviations of the dust density distribution from axisymmetry, which were also not taken into account by Milli et al. (2019) for their phase-curve fitting. The detailed extraction contains much more information on the nonsymmetric disk brightness distribution which is discussed in detail in Milli et al. (2019). Also, small-scale structures are seen in the extracted azimuthal polarization curve of HR 4796A for which the quadrant parameters are “blind”.

However, the HR 4796A example shows that the analysis on the quadrant polarization parameters performs rather well for high-quality data of a bright target if we are “only” interested in the global azimuthal polarization dependence of debris disks

caused by the polarized scattering phase function $f_{\phi}(\theta)$ of the dust.

6.3. Limitations

The quadrant polarization parameters are designed for a simple description and analysis of the azimuthal dependence of the scattering polarization of circumstellar disks. The method is well defined but it has limitations, which must be taken into account in the interpretation of the results.

Importantly, one should be aware that real disks are often quite complex and a description using only eight parameters or less only yields rough information about the left–right disk asymmetry and the differences in the front–back brightness distribution. There are various effects that can cause significant departures from axisymmetry in the disk geometry: an intrinsic ellipticity introduced by noncircular orbits of dust particles, different types of hydrodynamic instabilities introducing spiral structures, azimuthal density features, lopsided disks, shadows cast by unresolved dust structures near the central star, dynamical interactions with proto-planets or other gravitating bodies in the system, and probably other effects.

Such asymmetries can be identified easily as left–right differences but they can also produce brightness effects between the disk front- and backside which are then blended with front–back brightness effects caused by the dust-scattering asymmetry in optically thin disks or the angle-dependent surface reflectivity in optically thick disks.

For a disk with complex morphology based on a small number of measured polarization quadrant parameters, it can be difficult to recognize whether the asymmetries are caused by the disk geometry, the scattering phase function, optical depth effects, or an observational problem. Therefore, it is certainly always useful to examine the disk polarization images for the presence of strong azimuthal structures which can be taken into account for disentangling the effects of the disk geometry from those of the dust scattering phase function for an interpretation of the data.

Using only eight quadrant polarization parameters for the characterization of the detailed structure of a well-observed disk can of course only provide limited information as demonstrated for HR 4796A. In such a case, a detailed extraction of the polarized flux or a two-dimensional model fitting to the data as in Milli et al. (2019) or Arriaga et al. (2020) will provide more accurate results and a less ambiguous interpretation. For example, a detailed model analysis for HR 4796A could consider two or three parameters for the intensity scattering phase function $f_I(\theta)$, one or two parameters for the shape of the fractional scattering polarization $p_{\text{sca}}(\theta)$ (and not only the fixed Rayleigh scattering like curve given in Eq. 20), a description of the ring geometry, and three or more parameters for the azimuthal dust density distribution.

Therefore, the quadrant polarization parameters are less suitable for a detailed investigation of well-observed disks, and are more suitable for the exploration and the approximate description of the global properties of the scattering dust in many disks. However, it is still useful to derive these parameters for well-observed disk prototypes for a comparison with disks for which a detailed analysis is hardly possible, or for multi-wavelength studies of a given disk where a few well-defined parameters are sufficient to recognize and quantify wavelength dependencies for the polarized dust scattering phase function.

6.4. Conclusions

The quadrant polarization parameters introduced in this work seem to be very useful for a simple description of the azimuthal dependence of the polarization signal of circumstellar disks. These parameters can be determined from observations of many different types of circumstellar disks, for example debris disks around young or old stars, with or without strong illumination or dust blow-out signatures, or for proto-planetary disks with small or large central cavities and different kinds of hydrodynamical features.

The measured quadrant parameters can be compared with disk models that take the PSF smearing and cancellation effects into account and can explore the expected polarization signatures introduced by different descriptions for the scattering dust. Accumulating such data for a larger sample will allow a search for systematic trends in dust scattering properties for different disk types and for different wavelengths and inform us about the homogeneity or heterogeneity of dust-scattering properties in circumstellar disks. This can be achieved with relatively small uncertainties when compared to circumstellar shells or clouds, because the scattering angles θ , which have an important impact on the produced polarization signal, are typically very well known for resolved circumstellar disks. Investigations of the dust in circumstellar disks are also very attractive because many studies indicate that the dust evolves strongly in these systems and this could produce systematic trends for different disk types, which could be measurable with the new generation of AO polarimeters.

Acknowledgements. I am very grateful to Julien Milli for the reduced Q_{ϕ} and U_{ϕ} images of HR 4796A used in this study, for the polarized scattering phase curves derived in Milli et al. (2019), and for many useful comments on an earlier version of this manuscript. I am indebted to an anonymous referee who made a very detailed and thoughtful review of the submitted manuscript which helped to improve the final paper significantly. I also thank Jie Ma for a careful reading of the manuscript and for checking the mathematical formulas. This work has been carried out within the framework of the National Center for Competence in Research PlanetS supported by the Swiss National Science Foundation.

References

- Apai, D., Pascucci, I., Brandner, W., et al. 2004, *A&A*, 415, 671
 Arriaga, P., Fitzgerald, M. P., Duchêne, G., et al. 2020, *AJ*, 160, 79
 Artymowicz, P., Burrows, C., & Paresce, F. 1989, *ApJ*, 337, 494
 Avenhaus, H., Quanz, S. P., Garufi, A., et al. 2018, *ApJ*, 863, 44
 Bastien, P. 1982, *A&AS*, 48, 153
 Bastien, P. & Ménard, F. 1988, *ApJ*, 326, 334
 Benisty, M., Juhasz, A., Boccaletti, A., et al. 2015, *A&A*, 578, L6
 Beuzit, J. L., Vigan, A., Mouillet, D., et al. 2019, *A&A*, 631, A155
 Buenzli, E. & Schmid, H. M. 2009, *A&A*, 504, 259
 Canovas, H., Ménard, F., de Boer, J., et al. 2015, *A&A*, 582, L7
 Cantalloube, F., Dohlen, K., Milli, J., Brandner, W., & Vigan, A. 2019, *The Messenger*, 176, 25
 Chen, C., Mazoyer, J., Poteet, C. A., et al. 2020, *ApJ*, 898, 55
 de Boer, J., Langlois, M., van Holstein, R. G., et al. 2020, *A&A*, 633, A63
 Debes, J. H., Weinberger, A. J., & Kuchner, M. J. 2009, *ApJ*, 702, 318
 Engler, N., Schmid, H. M., Thalmann, C., et al. 2017, *A&A*, 607, A90
 Esposito, T. M., Kalas, P., Fitzgerald, M. P., et al. 2020, *AJ*, 160, 24
 Garufi, A., Quanz, S. P., Schmid, H. M., et al. 2016, *A&A*, 588, A8
 Graham, J. R., Kalas, P. G., & Matthews, B. C. 2007, *ApJ*, 654, 595
 Hashimoto, J., Tamura, M., Muto, T., et al. 2011, *ApJ*, 729, L17
 Heikamp, S. & Keller, C. U. 2019, *A&A*, 627, A156
 Henyey, L. G. & Greenstein, J. L. 1941, *ApJ*, 93, 70
 Hughes, A. M., Duchêne, G., & Matthews, B. C. 2018, *ARA&A*, 56, 541
 Hunziker, S., Schmid, H. M., Ma, J., et al. 2021, *A&A*, 648, A110
 Kalas, P. & Jewitt, D. 1996, *AJ*, 111, 1347
 Kolokolova, L. & Kimura, H. 2010, *A&A*, 513, A40
 Macintosh, B., Graham, J. R., Ingraham, P., et al. 2014, *Proceedings of the National Academy of Science*, 111, 12661
 Maness, H. L., Kalas, P., Peek, K. M. G., et al. 2009, *ApJ*, 707, 1098

- Milli, J., Engler, N., Schmid, H. M., et al. 2019, A&A, 626, A54
 Milli, J., Vigan, A., Mouillet, D., et al. 2017, A&A, 599, A108
 Min, M., Rab, C., Woitke, P., Dominik, C., & Ménard, F. 2016, A&A, 585, A13
 Monnier, J. D., Harries, T. J., Bae, J., et al. 2019, ApJ, 872, 122
 Muto, T., Grady, C. A., Hashimoto, J., et al. 2012, ApJ, 748, L22
 Olofsson, J., Milli, J., Bayo, A., Henning, T., & Engler, N. 2020, A&A, 640, A12
 Oppenheimer, B. R., Brenner, D., Hinkley, S., et al. 2008, ApJ, 679, 1574
 Perrin, M. D., Duchene, G., Millar-Blanchaer, M., et al. 2015, ApJ, 799, 182
 Perrin, M. D., Schneider, G., Duchene, G., et al. 2009, ApJ, 707, L132
 Quanz, S. P., Schmid, H. M., Geissler, K., et al. 2011, ApJ, 738, 23
 Schmid, H. M. 2021, IAU Symposium, 360, in press
 Schmid, H. M., Bazzon, A., Roelfsema, R., et al. 2018, A&A, 619, A9
 Schmid, H. M., Joos, F., & Tschan, D. 2006, A&A, 452, 657
 Schneider, G., Debes, J. H., Grady, C. A., et al. 2018, AJ, 155, 77
 Schneider, G., Weinberger, A. J., Becklin, E. E., Debes, J. H., & Smith, B. A. 2009, AJ, 137, 53
 Simmons, J. F. L. & Stewart, B. G. 1985, A&A, 142, 100
 Tazaki, R., Tanaka, H., Muto, T., Kataoka, A., & Okuzumi, S. 2019, MNRAS, 485, 4951
 Thébault, P. 2009, A&A, 505, 1269
 Tschudi, C. & Schmid, H. M. 2021, arXiv e-prints, arXiv:2108.03102
 van Holstein, R. G., Girard, J. H., de Boer, J., et al. 2020, A&A, 633, A64
 Whitney, B. A. & Hartmann, L. 1992, ApJ, 395, 529
 Yudin, R. V. & Evans, A. 1998, A&AS, 131, 401

Appendix A: Radiation parameters for debris disks.

The following IDL procedure calculates disk-averaged scattering functions and normalized quadrant polarization parameters for flat, rotationally symmetric, and optical thin disks with HG and HG_{pol} scattering phase functions. Input parameters are the disk inclination in degrees $i_{deg} \in [0^\circ, 90^\circ]$ and the scattering asymmetry parameter $g \in]-1, +1[$. Output parameters are f_{iavg} for the disk averaged intensity scattering phase function $\langle f_I(i, g) \rangle$ (Eq. 37) and f_{phiavg} for the corresponding normalized function for the azimuthal polarization $\langle f_\phi^n(i, g) \rangle$ (Eq. 38). In addition, the procedure provides the five normalized quadrant polarization parameter $qpp[0]$, $qpp[1]$, $qpp[2]$, $qpp[3]$, and $qpp[4]$ corresponding to $Q_{000}^n(i, g)$, $U_{045}^n(i, g)$, $Q_{090}^n(i, g)$, $U_{135}^n(i, g)$ and $Q_{180}^n(i, g)$, respectively (Sect. 3.3). The Stokes Q_d phase function follows from the quadrant sum $\langle f_Q^n(i, g) \rangle = 2 \cdot Q_{180}^n + Q_{000}^n + Q_{090}^n$.

Table A.1. IDL procedure for the calculation of disk-averaged scattering functions and normalized quadrant polarization parameters.

```

pro quadrants, ideg, g, fiavg, fphiavg, qpp
incl = ideg*!pi/180. ; inclination  $i$  in radians
; array of disk azimuth angles  $\varphi_d$  for disk ring: 3600 point with [0, 0.1, .., 359.9] degrees in radians
phi_d = findgen(3600)*!pi/1800.
x = -sin(phi_d) ; x-sky for inclined disk ring
y = cos(incl)*cos(phi_d) ; y-sky
z = -sin(incl)*cos(phi_d) ; z along line of sight
phi = atan(-x,y) ; sky azimuth angle  $\phi_{xy}(\varphi_d, i)$  (Eq. 34)
theta = acos(z) ; scattering angle  $\theta(\varphi_d, i)$  (Eq.30)
; scattering intensity using HG-phase function  $4\pi f_I(\theta, g)$  (Eq. 19)
fi = (1.-g^2)/(1.+g^2-2.*g*cos(theta))^1.5 ;  $4\pi f_I(\varphi_d, i)$  (Fig. 6)
; polarized intensity using Rayleigh scattering splitting with  $p_{\max} = 1$  (Eqs. 21,22)
fper = fi/(1.+(cos(theta))^2) ;  $f_{\perp}$  or azimuthal intensity
fpar = fi*(cos(theta))^2 / (1.+(cos(theta))^2) ;  $f_{\parallel}$  or radial intensity
fphi = fper-fpar ;  $4\pi f_{\phi}(\varphi_d, i)$ : azimuthal polarization (Fig. 6)
fq = fphi*(-cos(2.*phi)) ;  $4\pi f_Q(\varphi_d, i)$  for Stokes  $Q_d$  (Fig. 7)
fu = fphi*(-sin(2.*phi)) ;  $4\pi f_U(\varphi_d, i)$  for Stokes  $U_d$  (Fig. 7)
; disk averaged scattering functions  $\langle f(i, g) \rangle$ 
fiavg = mean(fi) ; intensity  $\langle f_I(i, g) \rangle$  (Eq. 37)
fphiavg = mean(fphi) ; azimuthal polarization  $\langle f_{\phi}(i, g) \rangle$  (Eq. 38)
; normalized quadrant polarization parameters
qpp = fltarr(5) ; initialize quadrant values
; sum-up of relevant  $\phi_{xy}(\varphi_d, i)$ -points for each quadrant (according to Tab. 2)
for j=0,3599 do begin
if (phi[j] gt -0.25*!pi and phi[j] lt 0.25*!pi) then qpp[0]=qpp[0]+fq[j]/3600. ; quadrant Q000
if (phi[j] gt 0. and phi[j] lt 0.50*!pi) then qpp[1]=qpp[1]+fu[j]/3600. ; quadrant U045
if (phi[j] gt 0.25*!pi and phi[j] lt 0.75*!pi) then qpp[2]=qpp[2]+fq[j]/3600. ; quadrant Q090
if (phi[j] gt 0.50*!pi and phi[j] lt 1.00*!pi) then qpp[3]=qpp[3]+fu[j]/3600. ; quadrant U135
if (phi[j] gt 0.75*!pi or phi[j] lt -0.75*!pi) then qpp[4]=qpp[4]+fq[j]/3600. ; quadrant Q180
endfor
return
end

```